bioRxiv preprint doi: https://doi.org/10.1101/2022.12.15.520527; this version posted December 15, 2022. The copyright holder for this preprint (which was not certified by peer review) is the author/funder, who has granted bioRxiv a license to display the preprint in perpetuity. It is made available under aCC-BY-NC-ND 4.0 International license.

Classification: Biological Sciences/Neuroscience

Title: Structural connectome architecture shapes the maturation of cortical morphology from childhood to adolescence

Author affiliations: Xinyuan Liang [a,b,c], Lianglong Sun[a,b,c], Xuhong Liao[d], Tianyuan Lei[a,b,c], Mingrui Xia[a,b,c], Dingna Duan[a,b,c], Zilong Zeng[a,b,c], Zhilei Xu [a,b,c], Weiwei Men[e,f], Yanpei Wang[a], Shuping Tan[g], Jia-Hong Gao[e,f,h], Shaozheng Qin [a,b,c,i], Sha Tao[a], Qi Dong[a], Tengda Zhao[a,b,c,*], Yong He[a,b,c,i,*]

[a] State Key Laboratory of Cognitive Neuroscience and Learning, Beijing Normal University, Beijing 100875, China;

[b] Beijing Key Laboratory of Brain Imaging and Connectomics, Beijing Normal University, Beijing 100875, China;

[c] IDG/McGovern Institute for Brain Research, Beijing Normal University, Beijing 100875, China;

[d] School of Systems Science, Beijing Normal University, Beijing 100875, China;

[e] Center for MRI Research, Academy for Advanced Interdisciplinary Studies, Peking University, Beijing 100871, China;

[f] Beijing City Key Laboratory for Medical Physics and Engineering, Institute of Heavy Ion Physics, School of Physics, Peking University, Beijing 100871, China;

[g] Beijing Huilongguan Hospital, Peking University Huilongguan Clinical Medical School, Beijing 100096, China;

[h] IDG/McGovern Institute for Brain Research, Peking University, Beijing 100871, China;

[i] Chinese Institute for Brain Research, Beijing 102206, China.

Corresponding authors:

Yong He, Ph.D., E-mail: yong.he@bnu.edu.cn
Tengda Zhao Ph.D., E-mail: tengdazhao@bnu.edu.cn

Keywords: brain development; white matter; connectomics; cortical thickness; MRI

Manuscript information: 24 text pages, 4 figures.
(Supplementary Information: 33 text pages, 11 figures, 8 tables.)

bioRxiv preprint doi: https://doi.org/10.1101/2022.12.15.520527; this version posted December 15, 2022. The copyright holder for this preprint (which was not certified by peer review) is the author/funder, who has granted bioRxiv a license to display the preprint in perpetuity. It is made available under aCC-BY-NC-ND 4.0 International license.

Abstract

Prior research indicates substantial refinements of regional cortical morphology in the transition period from childhood to adolescence. However, whether and how the spatial pattern of cortical maturation is shaped by underlying white matter connectome architecture remains largely unknown. Here, we address this issue by leveraging 521 longitudinal structural and diffusion magnetic resonance imaging scans from 314 typically developing individuals during childhood and adolescence (aged 6-14 years). We demonstrate widespread cortical thinning from childhood to adolescence predominantly distributed in bilateral frontoparietal heteromodal nodes, and this maturation pattern is structurally constrained by the white matter connectome architecture of the brain. Specifically, this constraint is first observed as a direct association of the cortical maturation extents between nodes and their anatomically connected neighbors. Using a network-level diffusion computational model, we further demonstrate that the spatial maturation of cortical thickness can be significantly predicted by using multiscale diffusion profiles of network links. Furthermore, these connectome-based constraints are primarily dominated by several core nodes located in bilateral frontoparietal regions, which exhibit differential gene expression profiles in microstructural neurodevelopment processes compared to non-dominant brain nodes. These findings are highly reproducible when using another independent neuroimaging dataset from the Lifespan Human Connectome Project in Development (aged 5-14 years). Our results highlight the importance of white matter network structure in shaping the coordinated maturation of regional cortical morphology and demonstrate the feasibility of using a network-based diffusion model to reveal the maturational principle of cortical morphology from childhood to adolescence.

bioRxiv preprint doi: https://doi.org/10.1101/2022.12.15.520527; this version posted December 15, 2022. The copyright holder for this preprint (which was not certified by peer review) is the author/funder, who has granted bioRxiv a license to display the preprint in perpetuity. It is made available under aCC-BY-NC-ND 4.0 International license.

Significance Statement

Cortical thinning is an important hallmark of the maturation of brain morphology during childhood and adolescence. However, the connectome-based wiring mechanism that underlies cortical maturation remains unclear. Using neuroimaging, connectome, transcriptome, and computational modeling, we mapped cortical thinning patterns primarily located in lateral frontal and parietal heteromodal nodes during childhood and adolescence, which is structurally constrained by white matter network architecture and is particularly represented using a network-based diffusion model. Furthermore, connectome-based constraints are regionally heterogeneous, with the largest constraints residing in frontoparietal nodes, and are associated with gene expression signatures of microstructural neurodevelopmental events. These findings advance our understanding of network-level mechanisms and the associated genetic basis that underlie the maturational process of cortical morphology during childhood and adolescence.

bioRxiv preprint doi: https://doi.org/10.1101/2022.12.15.520527; this version posted December 15, 2022. The copyright holder for this preprint (which was not certified by peer review) is the author/funder, who has granted bioRxiv a license to display the preprint in perpetuity. It is made available under aCC-BY-NC-ND 4.0 International license.

Introduction

The transition period from childhood to adolescence is characterized by prominent reorganization in cortical morphology (1, 2), which provides critical support for cognitive growth (3, 4). With progress in modern *in vivo* structural brain imaging, researchers have documented widespread spatial refinements of cortical morphology throughout childhood to adolescence (5, 6). A typical cortical maturation sequence is marked by hierarchical cortical thinning from the primary to association cortex (1, 7, 8) and is thought to be mediated by cellular mechanisms, genetic regulation, and biomechanical factors (9, 10). In the present study, we present a mechanistic approach to model how the maturational pattern of cortical morphology from childhood to adolescence is shaped by white matter (WM) connectome architecture.

At the microscale level, a large quantity of histological studies has suggested that the brain's WM pathways are involved in the developmental process of cortical gray matter. During neural circuit formation, axons express guidance receptors to integrate attractive and repulsive environmental information for navigation to their target neurons (11, 12). After axons arrive, synaptic maintenance and plasticity rely on active axonal transport through axonal cytoskeletons, which offers essential delivery of neurotrophic factors, energy requirements, and synthesized or degraded proteins for long distanced cortical neurons (13-15). Such early-established neuronal pathways could lead to preferences in attracting or removing new links during the formation of cortical hubs (16). Physical simulation studies suggest that there may be a tension-induced relationship between fiber growth and cortical fold morphology (17, 18). At a macroscale level, several prior studies using structural and diffusion magnetic resonance imaging (MRI) have also shown that focal cortical thickness (CT) decreases in the frontal cortex are associated with increased microstructural integrity in adjacent WM (19) and that homologous cortical regions, which are rich in WM fibers, exhibit higher maturational couplings of CT than nonhomologous regions (20). Notably, all these previous studies are limited to local cortical regions or certain fiber tracts. The human brain is a highly interacting network in nature in which connections promote interregional communications, raising the possibility that the maturation of focal cortical morphology is shaped by the overall architecture of the WM connectome. However, whether and how the maturation pattern of cortical morphology from childhood to adolescence is constrained by physical network structures, and specifically, whether this constraint works following a network-based diffusion model, remains largely unknown. We anticipate that models of regional cortical maturation would yield mechanistic insights into network structure that govern the coordinated development of cortical morphology among regions.

If the connectome structure shapes regional cortical maturation, it is necessary to further clarify whether this constraint is associated with genetic factors. Converging evidence indicates that genetic modulations may exist on the potential constraint of WM maturation on cortical morphology. Studies on the rodent nervous system (21, 22) have shown that the wiring diagram of brains is tracked by genes that are involved in axon guidance and neuronal development processes. Such genetic cues are also related to molecules responsible for cytoskeletal rearrangements that induce cortical refinement processes, including synaptic pruning and neuron cell death (12). In humans, recent emerging transcriptome imaging analyses pave a new way to link brain macroscale structural maturation to microscale biological processes by seeking associations between MRI-based brain measurements and genetic samples of postmortem brains. Such studies have shown that cortical thinning during maturation is related to genes involved in

bioRxiv preprint doi: https://doi.org/10.1101/2022.12.15.520527; this version posted December 15, 2022. The copyright holder for this preprint (which was not certified by peer review) is the author/funder, who has granted bioRxiv a license to display the preprint in perpetuity. It is made available under aCC-BY-NC-ND 4.0 International license.

the structure and function of synapses, dendrites, and myelin (23, 24). These precisely programmed microstructural alterations constitute major neurodevelopmental events that promote the establishment of more mature brain architecture and anatomical connectivity from childhood to adolescence (25, 26). Therefore, we further hypothesize that the constraint between the maturation of cortical morphology and WM network structure is associated with gene expression profiles that are involved in neurodevelopment.

To fill these gaps, in the present study, we integrated neuroimaging, connectome, and transcriptome analyses as well as computational modeling to investigate network-level associations with regional maturation of cortical morphology and to further explore their potential genetic underpinnings. Specifically, we test three hypotheses: (*i*) that the maturation of CT of brain nodes is associated with that of structurally connected neighbors, (*ii*) that the network-level diffusion model, which represents the direct and high-order information exchange preferences among neighbors, captures the principle of connectome constraint on the maturation of CT, and (*iii*) that the connectome constraints on cortical maturation are associated with gene expression levels of neurodevelopment processes.

Results

Data Samples

To investigate the relationship between cortical morphology maturation and the WM connectome from childhood to adolescence, we leveraged structural and diffusion MRI data from a longitudinal MRI dataset ("Discovery dataset") with 521 scans (314 participants, aged 6-14 years) in the Children School Functions and Brain Development Project in China (Beijing Cohort). According to the criteria from a previous public health investigation (27) and the World Health Organization (WHO) (28), we divided all participants into the child group (218 participants, 299 scans, 6.08-9.98 y) and the adolescent group (162 participants, 222 scans, 10.00-13.99 y) using age 10 years as a cutoff. To assess the reproducibility of our results, we also included an independent dataset ("Replication dataset") that contains structural and diffusion MRI data of 301 typically developing participants, which were divided into the child group (98 participants, 5.58-9.92 y) and in the adolescent group (203 participants, 10.00-14.00 y) from the Lifespan Human Connectome Project in Development (HCP-D) (29). Details of the demographic information for all participants, data acquisition, and data analysis are provided in the *SI Appendix*, Section 1.1-1.3.

The Typical Spatial Refinement of Brain CT from Childhood to Adolescence

For each individual, we first parcellated the brain cortex into 1000 nodes of interest with approximately equal size (219 and 448 nodes parcellations as a validation (30)) according to the modified Desikan-Killiany atlas (31, 32). Then, we computed the average CT for each brain node based on structural MR images. To delineate the spatial maturation map of brain morphology, we estimated the statistical differences in CT between the child and adolescent groups to represent the CT maturation extent by a mixed linear analysis (33) with sex included as the covariate (*SI Appendix*, Section 1.4). Brain nodes showed significant cortical thinning, mainly concentrated in dorsolateral prefrontal regions and lateral temporal and lateral parietal regions (Fig. 1A, *t*-values > 4.10, $P < 0.05$, Bonferroni corrected). To test whether this maturation pattern is anchored to specific brain systems, we classified all cortical nodes into seven well-validated

bioRxiv preprint doi: https://doi.org/10.1101/2022.12.15.520527; this version posted December 15, 2022. The copyright holder for this preprint (which was not certified by peer review) is the author/funder, who has granted bioRxiv a license to display the preprint in perpetuity. It is made available under aCC-BY-NC-ND 4.0 International license.

brain communities (34) and performed a spherical projection null test ("spin test") to correct for spatial autocorrelations by permuting seven communities positions 1000 times (35, 36). The class-specific mean *t*-values were expressed as *z* scores relative to this null model. We found that all brain systems showed decreased CT with development on average. The frontoparietal (FP) system and default mode (DM) system showed higher cortical thinning than expected by chance (FP: $p_{spin} = 0.029$; DM: $p_{spin} = 0.068$, Fig. 1B). The somatomotor (SM) system displayed lower cortical thinning than expected by chance ($p_{spin} = 0.004$). We also repeated this analysis by classifying cortical nodes into four laminar differentiation levels (37). We found that heteromodal areas displayed cortical thinning ($p_{spin} < 0.001$), while idiotypic areas showed lower cortical thinning than expected by chance ($p_{spin} = 0.001$, Fig. 1C). Consistent results were found at the other two parcellation resolutions (*SI Appendix*, Figs. S1-S2). These results are largely compatible with previous studies (1, 8), demonstrating that CT exhibits the most pronounced thinning in high-order association areas and is relatively preserved in primary areas from childhood to adolescence.

Direct WM Connections Constrain the Spatial Maturation of CT

Next, we tested whether the regional maturation of CT was constrained by its direct WM connections. To this end, we first reconstructed individual structural connectomes with 1000 nodes (219 and 448 nodes as a validation) based on diffusion MR images of the child group by performing deterministic tractography between cortical regions (38, 39). We then generated a binary, group-level connectome by using a consensus approach that preserves the connection length distributions of individual networks (40) (Fig. 2A, *SI Appendix*, Section 2.1).

Next, we estimated the across-node relationship of the CT maturation extent (*t*-value between child and adolescent groups) between a node and its directly connected neighbor nodes in the backbone (Fig. 2B) (*SI Appendix*, Section 2.2). We found a significant spatial correlation between the nodal CT maturation extent and the mean of its directly connected neighbors (Fig. 2C, adjusted $r = 0.74$, $P = 5.56\times10^{-176}$). Next, we tested this spatial correlation against two baseline null models (*SI Appendix*, Section 2.3). The first model evaluated whether the observed correlation was determined by the wiring topology rather than the basic spatial embedding of the WM network (41). Specifically, we generated 1000 surrogate networks by randomly rewiring edges while preserving the nodal degree and approximate edge length distribution of the empirical WM network ("rewired"). The second model evaluated whether the observed correlation was induced by the regional correspondence rather than the spatial autocorrelation of CT maturation (35, 36). Specifically, we generated 1000 surrogate maps by rotating region-level cortical *t*-values ("spin test"). After recalculating the correlation coefficient, we found that the observed correlation was significantly higher than the correlations in both null models, and these results were highly consistent for all three nodal resolutions (all $p_{rewired} < 0.001$ and all $p_{spin} < 0.001$, Fig. 2D). Interestingly, when estimating the spatial constraints at the system level, we found that direct WM connections within the heteromodal area, especially within and between FP and DM networks, showed strong constraints on the maturation of CT (Fig. 2E).

Considering that spatially adjacent nodes may intrinsically exhibit similar cortical development trends, we further performed another two confounding analyses to demonstrate that the observed correlation is not determined by the spatial proximity effect. In the first analysis, we excluded all spatially adjoining neighbors and recalculated the mean CT maturation extent of the remaining

bioRxiv preprint doi: https://doi.org/10.1101/2022.12.15.520527; this version posted December 15, 2022. The copyright holder for this preprint (which was not certified by peer review) is the author/funder, who has granted bioRxiv a license to display the preprint in perpetuity. It is made available under aCC-BY-NC-ND 4.0 International license.

structurally connected neighbors for each brain region ("excluded"). In the second analysis, we regressed out the effect of nodal mean Euclidean distance to its connected neighbors from the mean CT maturation extent ("regressed"). After re-estimating the empirical correlation coefficient (1000-node: adjusted $r_{excluded} = 0.60$ and adjusted $r_{regressed} = 0.74$), we repeated two null model tests and found consistent results at all three nodal resolutions (all $p_{rewired} < 0.001$, $p_{spin} < 0.001$, *SI Appendix*, Fig. S3).

Collectively, these results provided strong evidence from a network level that the spatial pattern of nodal CT maturation is structurally constrained by the underlying WM network topology.

The Diffusion Model of the WM Connectome Predicts the Spatial Maturation of CT

To further understand the mechanisms of how the maturation process of cortical morphology is constrained by the WM connectome, we proposed a graph-based diffusion model to simulate the network-level axonal interactions during cortical development. The nodal diffusion processes through multiscale WM edge paths are used to predict the maturation of cortical CT (*SI Appendix*, Section 2.4). Specifically, we first calculated the diffusive probabilities of a given node to other nodes during a random walk modeling with *nth* moving steps (for a toy, see Fig. 3A) to represent the nodal diffusion profile at *nth* neighboring scales ($n = 1, 2, 3, \ldots N$; the maximum neighboring scales N was set as the network diameter, which is the max shortest path length). Increasing moving steps present expansion scales of the probed neighborhood, which indicates local to distributed preferences of information exchange during the diffusion process. The diffusion profiles of all brain nodes form a diffusive probability matrix that represents the distribution of information propagation throughout the whole network. To further characterize the spatial layout of each diffusive matrix, we classified all cortical nodes into seven brain communities (34) and calculated the average diffusive probabilities within the same system and between different systems separately across brain nodes. Of note, we observed that the diffusion probabilities within the same cortical system were greater than 0.5 at the 1st scale and then decreasing with the expanding of neighboring scales (Fig. 3B). This indicates that a lower scale is mainly involved in more community segregation during propagation. Then, we trained a support vector regression (SVR) model with nodal diffusive profiles at each neighboring scale separately as input features to predict the CT maturation extent in a 10-fold cross-validation strategy (42). To evaluate the significance of prediction accuracy, we compared the empirical accuracy with two null model tests, including a spin test and a rewiring test. We found that the diffusive profiles of a given node could significantly predict its CT maturation extent at multiple neighboring scales ($r_{1\text{-}9\ scale}$: ranged from 0.65 to 0.75, all $p_{spin} <= 0.001$, all $p_{rewired} < 0.001$, Fig. 3C and *SI Appendix*, Table S1). The prediction accuracies are higher at lower neighboring scales. Additionally, features with high contribution of these predictions are mainly involved in the diffusion of frontal and parietal nodes (*SI Appendix*, Fig. S4). These results are highly consistent across all three nodal resolutions (*SI Appendix*, Fig. S5 and Tables S2-S3). Overall, our analysis of computational models indicates that the diffusive characteristics of WM connectome at the local to distance scales largely determine the spatial maturation map of CT from childhood to adolescence, with a relatively high effect among nodes within the same cortical system.

We next try to measure the dominant likelihood map for the spatial constraint between nodal CT maturation and WM connections and screen out brain nodes that lead the whole brain constraint (*SI Appendix*, Section 2.5). For each node, we calculated the cosine similarity between its diffusive profiles at the *nth* ($n = 1, 2, 3, \ldots, N$) scale and the CT maturation map (Fig. 3D). High

bioRxiv preprint doi: https://doi.org/10.1101/2022.12.15.520527; this version posted December 15, 2022. The copyright holder for this preprint (which was not certified by peer review) is the author/funder, who has granted bioRxiv a license to display the preprint in perpetuity. It is made available under aCC-BY-NC-ND 4.0 International license.

similarity of a node indicates that its neighboring diffusion preference largely resembled its neighboring distribution of CT maturation. We observed that the dominant likelihood maps are highly similar across all nine neighboring scales (Fig. 3E, top panel, *SI Appendix*, Fig. S6A) with high values in the bilateral prefrontal, parietal, and temporal regions. These regions were further identified as dominant nodes by higher similarity than expected by chance ($p_{spin} < 0.05$) (Fig. 3E, bottom panel, *SI Appendix*, Fig. S6B). The conjunction map of dominant nodes across all neighboring scales is shown in Fig. 3F, where the robust dominant nodes are mainly located in the bilateral prefrontal cortex and inferior parietal cortex. This indicates the leading roles of these regions in shaping the spatial maturation of whole brain CT. Similar results were found in other parcellation resolutions (*SI Appendix*, Fig. S7). To further verify these dominant nodes, we also used a different identification approach (43), which defines dominators as brain regions showing high maturation extents in both themselves and their directly connected neighbors (*SI Appendix*, Fig. S8A). Using this approach, we ranked nodes based on their CT maturation extents and their neighbors' mean CT maturation extents separately in ascending order and then calculated the mean rank of each node across both lists. Regions with significantly higher mean ranks ($p_{spin} < 0.05$) were identified as the dominant nodes. We found that this dominant likelihood map was significantly correlated with our network-based diffusion analysis (Spearman's $r = 0.81$, $p_{spin} < 0.001$, *SI Appendix*, Fig. S8B-C), with highly consistent dominant regions (*SI Appendix*, Fig. S8D).

To further exemplify the diffusion processes of the dominant nodes at each neighboring scale, we illustrated the diffusive profiles of the two most robust dominant nodes in the prefrontal (Fig. 3G, top panels) and inferior parietal (Fig. 3G, bottom panels) region, respectively. As the neighborhood scale expands, the diffusion of prefrontal dominators mainly spreads to neighbors within FP and DM systems, while the diffusion of parietal dominators mainly spreads to neighbors within DM, DA, and SM systems (Fig.S6C). These diffusion processes were mainly involved in nodes within the same system at low neighboring scales and in nodes between systems at high neighboring scales.

Regional Heterogeneous Constraints between CT Maturation and the Connectome Are Associated with Gene Expression Profiles

Next, we sought to explore the genetic associations of the nodal constraints between the spatial maturation of the CT and WM connectomes during development. We adopted the BrainSpan dataset (44) (*SI Appendix*, Section 3.1), which contains gene expression samples of brain tissues from 8 post-conception weeks to 40 years, to evaluate the regional genetic relevance. We selected four gene sets according to Kang and colleagues (26), which cover typical maturation procedures involved in both CT and WM, including axon development, myelination, dendrite development, and synapse development. We hypothesized that there should be differentiated transcriptomic characteristics between the identified dominant and non-dominant brain nodes. To this end, we first divided the cortical tissue samples into two categories according to whether they were dominant nodes in the conjunction map. Then, we calculated the first principal component score of each gene set's transcription level and estimated the category differences. The statistical significance was calculated by comparing the empirical difference against null differences generated by randomly resampling the same number of genes 1000 times from the remaining genes. We found divergent transcriptomic trajectories between dominant and non-dominant regions in all four maturation processes from childhood to adolescence (Fig. 4A), and

bioRxiv preprint doi: https://doi.org/10.1101/2022.12.15.520527; this version posted December 15, 2022. The copyright holder for this preprint (which was not certified by peer review) is the author/funder, who has granted bioRxiv a license to display the preprint in perpetuity. It is made available under aCC-BY-NC-ND 4.0 International license.

the transcription level in dominant regions was significantly higher than that in nondominant regions for dendrite ($P = 0.014$) and synapse development ($P = 0.002$) but significantly lower for axon development ($P < 0.001$) and myelination ($P < 0.001$) (Fig. 4B). This result indicates that gene expression could support the microstructural differences in neurodevelopment between dominant and non-dominant regions, resulting in a non-uniform degree of constraints between CT maturation and WM pathways.

Considering that the BrainSpan dataset only contains 11 sampling neocortex areas, we also validated the regional gene expression relevance by using Allen Human Brain Atlas datasets (45) *SI Appendix*, Section 3.2). After preprocessing with the abagen toolbox (46, 47), a matrix of gene expression profiles was generated (111 left brain regions × 8631 gene expression levels). Then, we identified the association between the dominant likelihood map and each gene expression map using Pearson's correlation and spin tests (1000 times). A total of 457 genes showed a positive correlation, and 619 genes showed a negative correlation ($p_{spin} < 0.05$, FDR corrected, *SI Appendix*, Table S6). Next, we performed Gene Ontology enrichment analysis (*SI Appendix*, Section 3.3) on these two gene sets using the ToppGene Suite (48). We found a significantly correlated gene list with positive correlations mainly enriched in learning or memory and synapse organization (biological process) as well as glutamatergic synapse, neuron spine, and somatodendritic compartment (cellular component) (all $P < 0.05$, FDR corrected, Fig. 4C, Fig. 4D) and negative correlations enriched in the generation of precursor metabolites and energy process (biological process) and myelin sheath components (cellular component) (all $P < 0.05$, FDR corrected, *SI Appendix*, Fig. S9). The detailed enrichment analysis results are shown in *SI Appendix*, Tables S7-S8.

Sensitivity and Replication Analyses

To validate the effectiveness of the WM connectome backbone, we used another diffusion imaging dataset with multishell diffusion gradients from HCP-D (29) to reconstruct the individual WM network and regenerate the group backbone. Using this new backbone, we found highly consistent results with our main findings. Specifically, nodal CT maturation extents are significantly correlated with their directly connected neighbors (adjusted $r = 0.76$, $p_{spin} < 0.001$, $p_{rewired} < 0.001$, *SI Appendix*, Fig. S10A). Using the network-based diffusion model, the spatial maturation of CT was also predicted by the diffusion properties of the WM network ($r_{1\text{-}8\ scale}$: ranged from 0.69 to 0.78, all $p_{spin} < 0.001$, $p_{rewired} < 0.001$, *SI Appendix*, Fig. S10B and *SI Appendix*, Table S4).

To evaluate the reproducibility of our findings, we replicated all main analyses using the Replication dataset from HCP-D. The results are highly consistent with those obtained using the Discovery dataset: (i) several heteromodal areas exhibited the most pronounced cortical thinning (*SI Appendix*, Fig. S11A); (ii) CT maturation extent of a node shows a positive correlation with the mean maturation extent of its directly connected neighbors (adjusted $r = 0.62$, adjusted $r_{excluded} = 0.46$, and adjusted $r_{regressed} = 0.62$), and the empirical correlation exceeded the values in null models (all $p_{spin} < 0.001$ and all $p_{rewired} < 0.001$, *SI Appendix*, Fig. S11B-D); (iii) the diffusion profiles of the WM network at multiple neighboring scales also predicted the spatial maturation of CT ($r_{1\text{-}4\ scale}$: ranged from 0.60 to 0.66, all $p_{spin} < 0.05$, $p_{rewired} < 0.001$, *SI Appendix*, Fig. S11E and *SI Appendix*, Table S5); and (iv) dominant nodes mainly reside in the lateral parietal regions (*SI Appendix*, Fig. S11F). Taken together, these findings provide replicable evidence that the WM network constrains the spatial maturation of CT from childhood to

bioRxiv preprint doi: https://doi.org/10.1101/2022.12.15.520527; this version posted December 15, 2022. The copyright holder for this preprint (which was not certified by peer review) is the author/funder, who has granted bioRxiv a license to display the preprint in perpetuity. It is made available under aCC-BY-NC-ND 4.0 International license.

adolescence.

Discussion

The present study shows for the first time the constraints of WM network architecture on the coordinated maturation of regional CT from childhood to adolescence and their associations with gene expression signatures. Specifically, we proposed a network-based diffusion model to predict regional cortical maturation from WM connectome architecture. These constraints are regionally heterogeneous and regulated by the gene expression of microstructural developmental processes. These results are largely consistent across three cortical parcellations and are highly reproducible across two independent datasets. Taken together, these findings provide insights into the understanding of network-level mechanisms that support the maturational process of cortical morphology.

Numerous previous studies have documented that the human brain undergoes remarkable refinements during childhood and adolescence, such as cortical thinning, area expansion, and WM myelination (2, 4, 7, 49, 50). These multifaced gray matter and WM changes have been proven to be intrinsically linked with each other at the regional level. For example, in early childhood, the spatial pattern of cortical surface area expansion during development is highly similar to the myelination of underlying cortico-cortical tracts (51). In children and adolescents, Jeon et al. (19) reported a significant correlation between the rate of CT decrease and the rate of FA increase in WM tracts at local gyri of the frontal lobe. In addition, tractography-based studies show that homologous cortical regions tightly connected by rich WM tracts show high CT maturation couplings (20). At the microscale level, cortical morphology changes during maturation are thought to have various biological origins, including synaptic pruning, increased axon diameter, and myelination (49, 52). Seeking a unified original model for the whole-brain cortical changes is difficult since even within the ventral temporal cortex, thinning of different brain regions seems to be due to distinguished factors (52). Here, we address this issue with a new perspective on brain network modeling. We showed that the morphology maturation of cortical nodes is well represented by that of their WM-connected neighbors during the transition from childhood to adolescence (Fig. 2B), and this association remained when we excluded the spatial proximity effect and validated it in an independent dataset (*SI Appendix*, Fig. S9). This network-level association is an important extension of previous developmental theories that support cortical thinning across brain development.

The WM network-based cortical maturation could be explained by several factors as follows. First, animal studies revealed that cortical regions that are structurally connected by axon projections are more likely sharing similar cytoarchitectures, such as neuronal density and laminar differentiation (53, 54). Moreover, higher cytoarchitectural similarity among regions tend to higher cortical coordinated maturations (55, 56) among neighboring nodes in the brain WM network. Second, a recent study using 19 different neurotransmitter receptors/transporters, such as dopamine and glutamate, found that structurally connected cortical regions usually show greater neurotransmitter receptor similarity (57). Therefore, these regions may be more inclined to be coregulated by similar physiological processes during development (58, 59). Third, direct WM connections facilitate ongoing interregional communication, enabling these regions to exhibit strong spontaneous neuronal activity couplings (60), which indicates the natural preference for the regional coordination of functional development. This also coincides with

bioRxiv preprint doi: https://doi.org/10.1101/2022.12.15.520527; this version posted December 15, 2022. The copyright holder for this preprint (which was not certified by peer review) is the author/funder, who has granted bioRxiv a license to display the preprint in perpetuity. It is made available under aCC-BY-NC-ND 4.0 International license.

Hebbian learning rule, where neurons that fire synchronously tend to form or consolidate connections between them (61, 62). Additionally, WM network-based constraints on cortical morphology exist extensively in adult brains. For instance, Gong et al. suggested that approximately 40% of edges in the adult CT covariance network show matched WM connections (63). In degenerative brain diseases, including schizophrenia, dementia, and Parkinson's disease, studies also found that the disease-related cortical deformation pattern across brain regions is conditioned by the WM network (43, 64, 65).

Notably, in this study, we proposed a network-based diffusive model for the constraint of WM on CT maturation. We highlight that nodal diffusion profiles of the WM connectome could accurately predict the maturation pattern of regional CT (Fig. 3B). From a physical transport perspective, the axonal microenvironment can be regarded as a porous medium that makes diffusion processes within brain tissues extremely critical for delivering oxygen and glucose during neuron metabolism (66). Meanwhile, diffusion of chemical neurotransmitters at synaptic clefts along axons is essential for forming postsynaptic responses during intercellular communications (67). At the macroscopic scale, network-based models have been proposed to simulate the consequences of interregional diffusive spread in latent topological space throughout the brain connectome. In neurodegenerative diseases (e.g., Alzheimer's disease), these models showed excellent prediction abilities for the spatial atrophy pattern of the cortex by capturing disrupted transport of trophic factors or accumulated spread of toxic misfolded proteins (68, 69). Based on brain images of nine very prematurely born infants, Friedrichs-Maeder et al. employed a diffusion model to explore the relationship between WM connectivities and cerebral MR measurements such as T1 relaxation time (70). They reported that early maturation in the primary sensory cortex serves as a source to gradually propagate into the higher-order cortex. In our study, considering the intricate biological relevance between brain WM and cortical morphology (49, 52), we used a simple random walk model to depict the complex network diffusive processes of brain nodes. This model can concisely present the local to distributed supports of the structural connectome on cortical maturation from childhood to adolescence. These nodal diffusive features are effectively integrated by a multivariable machine learning model to represent nodal cortical maturation. Of note, this model first showed the significance of indirectly WM-connected neighbors for constraining nodal morphology maturation, which strongly emphasizes the necessity of employing a network-level model to capture this relationship. The contribution from indirect neighboring scales is reasonable because cortical communications between brain regions inherently contain high-order components to support information exchanges between topologically distant nodes (71, 72). Meanwhile, these indirect WM neighbors are shown majorly located within nearby cortical communities (Fig.3B-C) that share common maturation processes to support morphological integration during cortical development (73, 74).

Our results also showed that the constraints of the WM network on CT maturation are spatially heterogeneous (Fig. 3B and Fig. 3D). Regionally, dominant nodes in the heteromodal area, especially within and between FP and DM networks, show the strongest spatial constraints. Previous neuroimaging studies have revealed that FP and DM networks display dramatic cortical thinning from childhood to adolescence (1, 8). During the same period, brain WM integrity (measured by fractional anisotropy) and functional connectivity also show prominently increased tendencies within these networks (75, 76). Our results imply that the strong WM constraints on the cortical maturation of the heteromodal area may determine the major pattern of whole-brain

bioRxiv preprint doi: https://doi.org/10.1101/2022.12.15.520527; this version posted December 15, 2022. The copyright holder for this preprint (which was not certified by peer review) is the author/funder, who has granted bioRxiv a license to display the preprint in perpetuity. It is made available under aCC-BY-NC-ND 4.0 International license.

cortical thinning. Compatible with our findings of connectome-morphology constraints, structure–function association studies also show age-related increases in heteromodal area during youth, which are associated with individual executive performance (77). These multifaced heteromodal refinements could support the rapid enhancement of high-order cognitive and social capabilities such as working memory and reasoning (76, 78).

By employing transcriptome imaging analyses in a developmental gene expression dataset, we found that those dominant nodes in the heteromodal area show different transcriptional patterns compared with non-dominant brain nodes. Specifically, dominant regions exhibit higher gene expression levels involved in the maturation of gray matter morphology, including synaptic and dendritic development, and lower expression levels associated with WM maturation, such as axon and myelin development. This coincides with the findings from histological samples and MR images studies, demonstrating that heteromodal regions have higher synaptic density and lighter myelination than other regions in childhood and adolescence. This brings prolonged maturation of high-order cortex during adolescence to support the optimization and consolidation of synaptic and axonal connectivity compatible with cognitive growth and the environment (1, 23, 25, 50). Likewise, we conducted GO enrichment analysis with the AHBA dataset, which is the most complete gene expression dataset available on the human brain to date, and found that the nonuniform degree of constraints is mainly related to the biological processes and cellular components involved in learning or memory, synapse organization, glutamatergic synapse, and neuron spine. These gene-related processes are involved in the spatial thinning of CT during childhood and adolescence (23, 24). As the most abundant synapse type in the neocortex, glutamatergic synapses are primarily responsible for the transport of excitatory transmitters, which are crucial for regulating the transmission and processing of information among brain regions (67). Meanwhile, neuron spines on dendrites serve to receive various kinds of excitatory inputs from axons and are considered crucial for brain circuit wiring distribution and circuit plasticity (79, 80). Disruptions of these synapses structures are important substrates of pathogenesis in multiple neurodevelopment diseases, especially those with deficits in information processing, such as autism (79, 81). In summary, our findings provide evidence that genetic factors associated with the microstructure development contribute to these connectome-based constraints on cortical maturation.

Several issues need further consideration. First, diffusive processes during axonal transport are proven directional (13). However, *in vivo* inference for the direction of WM fibers is still extremely difficult with tractography-based methods. Future investigations combining diffusion models with animal connectome by molecular tracers would reveal a directed network constraint mechanism. Second, the developmental gene data from BrainSpan only contain 11 areas of the neocortex (44), which can only provide a rough exploration of the differences in gene expression between dominant and non-dominant nodes. We further validated this result using the AHBA datasets (45), but it was sampled from only six postmortem adult brains. Future studies with gene expression data of widespread cortical regions from a large sample of children and adolescents would be important for connectome-transcriptome association analysis. Finally, we showed the constraints of the WM network on cortical morphology maturation in typical development. Previous studies have documented both abnormal cortical maturation and WM connectome structure in neurodevelopmental disorders such as autism (82) and attention-deficit/hyperactivity disorder (83). In the future, it would be desirable to examine how the WM connectome shapes cortical morphology in these atypical populations.

bioRxiv preprint doi: https://doi.org/10.1101/2022.12.15.520527; this version posted December 15, 2022. The copyright holder for this preprint (which was not certified by peer review) is the author/funder, who has granted bioRxiv a license to display the preprint in perpetuity. It is made available under aCC-BY-NC-ND 4.0 International license.

Materials and Methods

Participants and Data Acquisition

We performed analyses in two independent datasets. The Discovery Dataset included a longitudinal cohort of 314 participants (aged 6-14 years) with 299 scans in the child group (mean (± SD) age 8.68 ± 0.94 y, 157 females) and 222 scans in the adolescent group (mean age 11.19 ± 0.94 y, 108 females) from the Beijing Cohort in Children Brain Development (CBD) project (84). Structural and high angular resolution diffusion imaging (HARDI) diffusion MR brain images for each subject were scanned at Peking University using a 3T Siemens Prisma scanner. Informed written consent was obtained from all participants and at least one parent/guardian, consistent with the guidelines of the Ethics Committee of Beijing Normal University. The Replication Dataset included a cross-sectional cohort of 301 participants (aged 5-14 years) with 98 scans in the child group (mean age 8.72 ± 0.99 y, 32 females) and 203 scans in the adolescent group (mean age 12.17 ± 1.28 y, 86 females) selected from the Lifespan Human Connectome Project in Development (HCP-D) (29). Participants were recruited across four imaging sites, and details on imaging protocols can be found in (85).

Estimation of Regional CT and WM Networks

Each participant's cortex was parcellated into 1000 regional nodes with approximately equally sized based on the modified Desikan-Kiliany atlas (31, 32) and verified at 219-node and 448-node parcellations. The CT of each brain node was estimated by using FreeSurfer v6.0 software (https://surfer.nmr.mgh.harvard.edu/). Then, we reconstructed anatomical streamlines between each two cortical nodes based on diffusion MR images using generalized q-sampling imaging (GQI)-based deterministic streamline tractography (39, 86) and combined a consensus approach to generate the binary group-level WM connectome (40).

Data Analysis

We explored the relationship between cortical morphology maturation and WM networks by the following analysis. (i) To estimate the maturation of CT from childhood to adolescence, we applied a mixed linear analysis with the sex term included as the covariate and the group term as the main effect for each brain node. The T statistics from the group term were used to represent the maturation extent of brain nodes. (ii) To test whether the regional maturation of CT was constrained by its direct WM connections, we calculated the spatial correlation between the maturation extent of nodal CT and the mean t value of its directly WM-connected neighbors. (iii) We proposed a diffusion model by combining *nth*-order random walk processes with a support vector regression method to determine whether the diffusion properties of the WM network could predict the maturation pattern of CT. To further identify the dominant regions, which play more important roles in leading cortical development, we calculated the cosine similarity between the CT maturation map and the nodal diffusion profiles. (iv) We used developmental gene expression data from BrainSpan (44) to evaluate whether there are distinctions in the expression levels of genes associated with several neural development events between dominant and non-dominant regions. Four typical maturation gene sets (26) were selected covering axon development, myelination, dendrite development, and synapse development. To further validate the relationship between spatial heterogeneous constraints and cortical gene expression levels at the whole-brain level, we performed a Pearson's correlation analysis with Allen Human Brain

bioRxiv preprint doi: https://doi.org/10.1101/2022.12.15.520527; this version posted December 15, 2022. The copyright holder for this preprint (which was not certified by peer review) is the author/funder, who has granted bioRxiv a license to display the preprint in perpetuity. It is made available under aCC-BY-NC-ND 4.0 International license.

Atlas datasets (45) combined with Gene Ontology enrichment analysis.

Detailed information about participants, image acquisition, data preprocessing, and data analyses are further described in *SI Appendix*.

Data Availability

The Replication Dataset used here is from the Lifespan Human Connectome Project in Development (29), which is available for download through https://nda.nih.gov/. The BrainSpan Atlas dataset is available at http://brainspan.org/static/download.html (44). The AHBA dataset is available at https://human.brain-map.org/static/download (45). The study data and codes are available at https://github.com/Xinyuan-Liang/SC-shapes-the-maturation-of-cortical-morphology.

bioRxiv preprint doi: https://doi.org/10.1101/2022.12.15.520527; this version posted December 15, 2022. The copyright holder for this preprint (which was not certified by peer review) is the author/funder, who has granted bioRxiv a license to display the preprint in perpetuity. It is made available under aCC-BY-NC-ND 4.0 International license.

Acknowledgments

This work was supported by the National Key Research and Development Project (No. 2018YFA0701402), the National Natural Science Foundation of China (Nos. 82021004, 31830034, 31521063, 31221003), Changjiang Scholar Professorship Award (No. T2015027), the Beijing Brain Initiative of Beijing Municipal Science & Technology Commission (No. Z181100001518003) and the China Postdoctoral Science Foundation (2020TQ0050 and 2022M710433). We thank for Dr. Yongbin Wei for the discussion on gene expression data. We thank the National Center for Protein Sciences at Peking University in Beijing, China, for assistance with MRI data acquisition. We also thank the Allen Institute for Brain Science for providing the gene expression data. Research reported in this publication was supported by the National Institute of Mental Health of the National Institutes of Health under Award Number U01MH109589 and by funds provided by the McDonnell Center for Systems Neuroscience at Washington University in St. Louis. The content is solely the responsibility of the authors and does not necessarily represent the official views of the National Institutes of Health.

Author contributions:

X.Y.L., T.D.Z., and Y.H. designed research; W.W.M., Y.P.W., S.P.T., J.H.G., S.Z.Q., S.T., and Q.D. collected the imaging dataset; T.D.Z., L.L.S., X.H.L., T.Y.L., M.R.X., D.N.D., Z.L.Z., Z.L.X., and Y.H. provided the methodological instruction; X.Y.L. and T.D.Z. performed the data analysis; X.Y.L., T.D.Z., and Y.H. wrote the paper; X.Y.L., L.L.S., T.D.Z., and Y.H. revised the paper.

bioRxiv preprint doi: https://doi.org/10.1101/2022.12.15.520527; this version posted December 15, 2022. The copyright holder for this preprint (which was not certified by peer review) is the author/funder, who has granted bioRxiv a license to display the preprint in perpetuity. It is made available under aCC-BY-NC-ND 4.0 International license.

References

1. P. Shaw *et al.*, Neurodevelopmental trajectories of the human cerebral cortex. *Journal of neuroscience* **28**, 3586-3594 (2008).
2. I. K. Amlien *et al.*, Organizing Principles of Human Cortical Development--Thickness and Area from 4 to 30 Years: Insights from Comparative Primate Neuroanatomy. *Cereb Cortex* **26**, 257-267 (2016).
3. B. J. Casey, S. Getz, A. Galvan, The adolescent brain. *Developmental Review* **28**, 62-77 (2008).
4. P. Shaw *et al.*, Intellectual ability and cortical development in children and adolescents. *Nature* **440**, 676-679 (2006).
5. R. A. Bethlehem *et al.*, Brain charts for the human lifespan. *Nature* **604**, 525-533 (2022).
6. L. Foulkes, S.-J. Blakemore, Studying individual differences in human adolescent brain development. *Nature neuroscience* **21**, 315-323 (2018).
7. E. R. Sowell *et al.*, Longitudinal mapping of cortical thickness and brain growth in normal children. *Journal of neuroscience* **24**, 8223-8231 (2004).
8. S. Frangou *et al.*, Cortical thickness across the lifespan: Data from 17,075 healthy individuals aged 3–90 years. *Human brain mapping* **43**, 431-451 (2022).
9. J. Shin *et al.*, Cell-specific gene-expression profiles and cortical thickness in the human brain. *Cerebral Cortex* **28**, 3267-3277 (2018).
10. C. Llinares-Benadero, V. Borrell, Deconstructing cortical folding: genetic, cellular and mechanical determinants. *Nature Reviews Neuroscience* **20**, 161-176 (2019).
11. E. T. Stoeckli, Understanding axon guidance: are we nearly there yet? *Development* **145**, dev151415 (2018).
12. P. Vanderhaeghen, H.-J. Cheng, Guidance molecules in axon pruning and cell death. *Cold Spring Harbor perspectives in biology* **2**, a001859 (2010).
13. P. Guedes-Dias, E. L. Holzbaur, Axonal transport: Driving synaptic function. *Science* **366**, eaaw9997 (2019).
14. T. Paus, M. Pesaresi, L. French, White matter as a transport system. *Neuroscience* **276**, 117-125 (2014).
15. E. Perlson, S. Maday, M.-m. Fu, A. J. Moughamian, E. L. Holzbaur, Retrograde axonal transport: pathways to cell death? *Trends in neurosciences* **33**, 335-344 (2010).
16. M. Kaiser, Mechanisms of connectome development. *Trends in Cognitive Sciences* **21**, 703-717 (2017).
17. D. C. Van Essen, A 2020 view of tension-based cortical morphogenesis. *Proceedings of the National Academy of Sciences* **117**, 32868-32879 (2020).
18. K. E. Garcia, X. Wang, C. D. Kroenke, A model of tension-induced fiber growth predicts white matter organization during brain folding. *Nature communications* **12**, 1-13 (2021).
19. T. Jeon, V. Mishra, M. Ouyang, M. Chen, H. Huang, Synchronous changes of cortical thickness and corresponding white matter microstructure during brain development accessed by diffusion MRI tractography from parcellated cortex. *Frontiers in Neuroanatomy* **9**, 158 (2015).
20. A. Raznahan *et al.*, Patterns of coordinated anatomical change in human cortical development: a longitudinal neuroimaging study of maturational coupling. *Neuron* **72**, 873-884 (2011).
21. L. Wolf, C. Goldberg, N. Manor, R. Sharan, E. Ruppin, Gene expression in the rodent

bioRxiv preprint doi: https://doi.org/10.1101/2022.12.15.520527; this version posted December 15, 2022. The copyright holder for this preprint (which was not certified by peer review) is the author/funder, who has granted bioRxiv a license to display the preprint in perpetuity. It is made available under aCC-BY-NC-ND 4.0 International license.

brain is associated with its regional connectivity. *PLoS computational biology* **7**, e1002040 (2011).
22. L. French, P. Pavlidis, Relationships between gene expression and brain wiring in the adult rodent brain. *PLoS computational biology* **7**, e1001049 (2011).
23. K. J. Whitaker *et al.*, Adolescence is associated with genomically patterned consolidation of the hubs of the human brain connectome. *Proceedings of the National Academy of Sciences* **113**, 9105-9110 (2016).
24. N. Parker *et al.*, Assessment of neurobiological mechanisms of cortical thinning during childhood and adolescence and their implications for psychiatric disorders. *JAMA psychiatry* **77**, 1127-1136 (2020).
25. P. R. Huttenlocher, A. S. Dabholkar, Regional differences in synaptogenesis in human cerebral cortex. *Journal of comparative Neurology* **387**, 167-178 (1997).
26. H. J. Kang *et al.*, Spatio-temporal transcriptome of the human brain. *Nature* **478**, 483-489 (2011).
27. S. M. Sawyer, P. S. Azzopardi, D. Wickremarathne, G. C. Patton, The age of adolescence. *The Lancet Child & Adolescent Health* **2**, 223-228 (2018).
28. J. A. Singh, M. Siddiqi, P. Parameshwar, V. Chandra-Mouli, World Health Organization guidance on ethical considerations in planning and reviewing research studies on sexual and reproductive health in adolescents. *Journal of Adolescent Health* **64**, 427-429 (2019).
29. L. H. Somerville *et al.*, The Lifespan Human Connectome Project in Development: A large-scale study of brain connectivity development in 5-21 year olds. *Neuroimage* **183**, 456-468 (2018).
30. A. Zalesky *et al.*, Whole-brain anatomical networks: does the choice of nodes matter? *Neuroimage* **50**, 970-983 (2010).
31. R. S. Desikan *et al.*, An automated labeling system for subdividing the human cerebral cortex on MRI scans into gyral based regions of interest. *Neuroimage* **31**, 968-980 (2006).
32. L. Cammoun *et al.*, Mapping the human connectome at multiple scales with diffusion spectrum MRI. *Journal of neuroscience methods* **203**, 386-397 (2012).
33. N. M. Laird, J. H. Ware, Random-effects models for longitudinal data. *Biometrics*, 963-974 (1982).
34. B. T. Yeo *et al.*, The organization of the human cerebral cortex estimated by intrinsic functional connectivity. *Journal of neurophysiology* (2011).
35. A. F. Alexander-Bloch *et al.*, On testing for spatial correspondence between maps of human brain structure and function. *Neuroimage* **178**, 540-551 (2018).
36. F. Vasa *et al.*, Adolescent Tuning of Association Cortex in Human Structural Brain Networks. *Cereb Cortex* **28**, 281-294 (2018).
37. M.-M. Mesulam, Behavioral neuroanatomy. *Principles of behavioral and cognitive neurology* **2**, 1-120 (2000).
38. F.-C. Yeh, T. D. Verstynen, Y. Wang, J. C. Fernández-Miranda, W.-Y. I. Tseng, Deterministic diffusion fiber tracking improved by quantitative anisotropy. *PloS one* **8**, e80713 (2013).
39. G. Gong *et al.*, Mapping anatomical connectivity patterns of human cerebral cortex using in vivo diffusion tensor imaging tractography. *Cerebral cortex* **19**, 524-536 (2009).
40. R. F. Betzel, A. Griffa, P. Hagmann, B. Mišić, Distance-dependent consensus thresholds for generating group-representative structural brain networks. *Network neuroscience* **3**,

bioRxiv preprint doi: https://doi.org/10.1101/2022.12.15.520527; this version posted December 15, 2022. The copyright holder for this preprint (which was not certified by peer review) is the author/funder, who has granted bioRxiv a license to display the preprint in perpetuity. It is made available under aCC-BY-NC-ND 4.0 International license.

475-496 (2019).
41. R. F. Betzel, D. S. Bassett, Specificity and robustness of long-distance connections in weighted, interareal connectomes. *Proceedings of the National Academy of Sciences* **115**, E4880-E4889 (2018).
42. Z. Cui, G. Gong, The effect of machine learning regression algorithms and sample size on individualized behavioral prediction with functional connectivity features. *Neuroimage* **178**, 622-637 (2018).
43. G. Shafiei *et al.*, Spatial patterning of tissue volume loss in schizophrenia reflects brain network architecture. *Biological psychiatry* **87**, 727-735 (2020).
44. J. A. Miller *et al.*, Transcriptional landscape of the prenatal human brain. *Nature* **508**, 199-206 (2014).
45. M. J. Hawrylycz *et al.*, An anatomically comprehensive atlas of the adult human brain transcriptome. *Nature* **489**, 391-399 (2012).
46. A. Arnatkevičiūtė, B. D. Fulcher, A. Fornito, A practical guide to linking brain-wide gene expression and neuroimaging data. *Neuroimage* **189**, 353-367 (2019).
47. R. D. Markello *et al.*, Standardizing workflows in imaging transcriptomics with the abagen toolbox. *Elife* **10**, e72129 (2021).
48. J. Chen, E. E. Bardes, B. J. Aronow, A. G. Jegga, ToppGene Suite for gene list enrichment analysis and candidate gene prioritization. *Nucleic acids research* **37**, W305-W311 (2009).
49. K. B. Walhovd, A. M. Fjell, J. Giedd, A. M. Dale, T. T. Brown, Through thick and thin: a need to reconcile contradictory results on trajectories in human cortical development. *Cerebral Cortex* **27**, bhv301 (2016).
50. D. J. Miller *et al.*, Prolonged myelination in human neocortical evolution. *Proceedings of the National Academy of Sciences* **109**, 16480-16485 (2012).
51. R. Cafiero, J. Brauer, A. Anwander, A. D. Friederici, The concurrence of cortical surface area expansion and white matter myelination in human brain development. *Cerebral Cortex* **29**, 827-837 (2019).
52. V. S. Natu *et al.*, Apparent thinning of human visual cortex during childhood is associated with myelination. *Proceedings of the National Academy of Sciences* **116**, 20750-20759 (2019).
53. S. F. Beul, H. Barbas, C. C. Hilgetag, A predictive structural model of the primate connectome. *Scientific reports* **7**, 1-12 (2017).
54. S. F. Beul, S. Grant, C. C. Hilgetag, A predictive model of the cat cortical connectome based on cytoarchitecture and distance. *Brain Structure and Function* **220**, 3167-3184 (2015).
55. J. K. Moore, Y.-L. Guan, Cytoarchitectural and axonal maturation in human auditory cortex. *Journal of the Association for Research in Otolaryngology* **2**, 297-311 (2001).
56. J. Gomez *et al.*, Microstructural proliferation in human cortex is coupled with the development of face processing. *Science* **355**, 68-71 (2017).
57. J. Y. Hansen *et al.*, Mapping neurotransmitter systems to the structural and functional organization of the human neocortex. *Nature Neuroscience* **25**, 1569-1581 (2022).
58. S. Mayer *et al.*, Multimodal single-cell analysis reveals physiological maturation in the developing human neocortex. *Neuron* **102**, 143-158. e147 (2019).
59. K. W. Kelley, S. P. Pașca, Human brain organogenesis: Toward a cellular understanding of development and disease. *Cell* (2021).

bioRxiv preprint doi: https://doi.org/10.1101/2022.12.15.520527; this version posted December 15, 2022. The copyright holder for this preprint (which was not certified by peer review) is the author/funder, who has granted bioRxiv a license to display the preprint in perpetuity. It is made available under aCC-BY-NC-ND 4.0 International license.

60. M. P. Van Den Heuvel, R. C. Mandl, R. S. Kahn, H. E. Hulshoff Pol, Functionally linked resting-state networks reflect the underlying structural connectivity architecture of the human brain. *Human brain mapping* **30**, 3127-3141 (2009).
61. D. O. Hebb, *The organization of behavior: a neuropsychological theory* (Science editions, 1949).
62. G. Koch, V. Ponzo, F. Di Lorenzo, C. Caltagirone, D. Veniero, Hebbian and anti-Hebbian spike-timing-dependent plasticity of human cortico-cortical connections. *Journal of Neuroscience* **33**, 9725-9733 (2013).
63. G. Gong, Y. He, Z. J. Chen, A. C. Evans, Convergence and divergence of thickness correlations with diffusion connections across the human cerebral cortex. *Neuroimage* **59**, 1239-1248 (2012).
64. G. Shafiei *et al.*, Network structure and transcriptomic vulnerability shape atrophy in frontotemporal dementia. *Brain* (2022).
65. Y.-Q. Zheng *et al.*, Local vulnerability and global connectivity jointly shape neurodegenerative disease propagation. *PLoS biology* **17**, e3000495 (2019).
66. C. Nicholson, Diffusion and related transport mechanisms in brain tissue. *Reports on progress in Physics* **64**, 815 (2001).
67. V. Di Maio, The glutamatergic synapse: a complex machinery for information processing. *Cognitive Neurodynamics* **15**, 757-781 (2021).
68. J. Zhou, E. D. Gennatas, J. H. Kramer, B. L. Miller, W. W. Seeley, Predicting regional neurodegeneration from the healthy brain functional connectome. *Neuron* **73**, 1216-1227 (2012).
69. A. Raj, A. Kuceyeski, M. Weiner, A network diffusion model of disease progression in dementia. *Neuron* **73**, 1204-1215 (2012).
70. C. L. Friedrichs-Maeder *et al.*, Exploring the role of white matter connectivity in cortex maturation. *PloS one* **12**, e0177466 (2017).
71. G. Rosenthal *et al.*, Mapping higher-order relations between brain structure and function with embedded vector representations of connectomes. *Nature communications* **9**, 1-12 (2018).
72. V. Bazinet, R. V. de Wael, P. Hagmann, B. C. Bernhardt, B. Misic, Multiscale communication in cortico-cortical networks. *NeuroImage* **243**, 118546 (2021).
73. B. A. Zielinski, E. D. Gennatas, J. Zhou, W. W. Seeley, Network-level structural covariance in the developing brain. *Proceedings of the National Academy of Sciences* **107**, 18191-18196 (2010).
74. A. Nadig *et al.*, Morphological integration of the human brain across adolescence and adulthood. *Proceedings of the National Academy of Sciences* **118**, e2023860118 (2021).
75. K. Supekar *et al.*, Development of functional and structural connectivity within the default mode network in young children. *Neuroimage* **52**, 290-301 (2010).
76. C. Wendelken, E. Ferrer, K. J. Whitaker, S. A. Bunge, Fronto-parietal network reconfiguration supports the development of reasoning ability. *Cerebral Cortex* **26**, 2178-2190 (2016).
77. G. L. Baum *et al.*, Development of structure–function coupling in human brain networks during youth. *Proceedings of the National Academy of Sciences* **117**, 771-778 (2020).
78. J. Liu *et al.*, Intrinsic brain hub connectivity underlies individual differences in spatial working memory. *Cerebral cortex* **27**, 5496-5508 (2017).
79. P. Penzes, M. E. Cahill, K. A. Jones, J.-E. VanLeeuwen, K. M. Woolfrey, Dendritic spine

bioRxiv preprint doi: https://doi.org/10.1101/2022.12.15.520527; this version posted December 15, 2022. The copyright holder for this preprint (which was not certified by peer review) is the author/funder, who has granted bioRxiv a license to display the preprint in perpetuity. It is made available under aCC-BY-NC-ND 4.0 International license.

pathology in neuropsychiatric disorders. *Nature neuroscience* **14**, 285-293 (2011).
80. R. Yuste, Dendritic spines and distributed circuits. *Neuron* **71**, 772-781 (2011).
81. L. Volk, S.-L. Chiu, K. Sharma, R. L. Huganir, Glutamate synapses in human cognitive disorders. *Annual review of neuroscience* **38**, 127-149 (2015).
82. C. Ecker, S. Y. Bookheimer, D. G. Murphy, Neuroimaging in autism spectrum disorder: brain structure and function across the lifespan. *The Lancet Neurology* **14**, 1121-1134 (2015).
83. X. Bu, M. Cao, X. Huang, Y. He, The structural connectome in ADHD. *Psychoradiology* **1**, 257-271 (2021).
84. T. Zhao *et al.*, Unbiased age-specific structural brain atlases for Chinese pediatric population. *Neuroimage* **189**, 55-70 (2019).
85. M. P. Harms *et al.*, Extending the Human Connectome Project across ages: Imaging protocols for the Lifespan Development and Aging projects. *Neuroimage* **183**, 972-984 (2018).
86. F.-C. Yeh, V. J. Wedeen, W.-Y. I. Tseng, Generalized *q*-sampling imaging. *IEEE transactions on medical imaging* **29**, 1626-1635 (2010).
87. M. Xia, J. Wang, Y. He, BrainNet Viewer: a network visualization tool for human brain connectomics. *PloS one* **8**, e68910 (2013).

bioRxiv preprint doi: https://doi.org/10.1101/2022.12.15.520527; this version posted December 15, 2022. The copyright holder for this preprint (which was not certified by peer review) is the author/funder, who has granted bioRxiv a license to display the preprint in perpetuity. It is made available under aCC-BY-NC-ND 4.0 International license.

Figure Legends

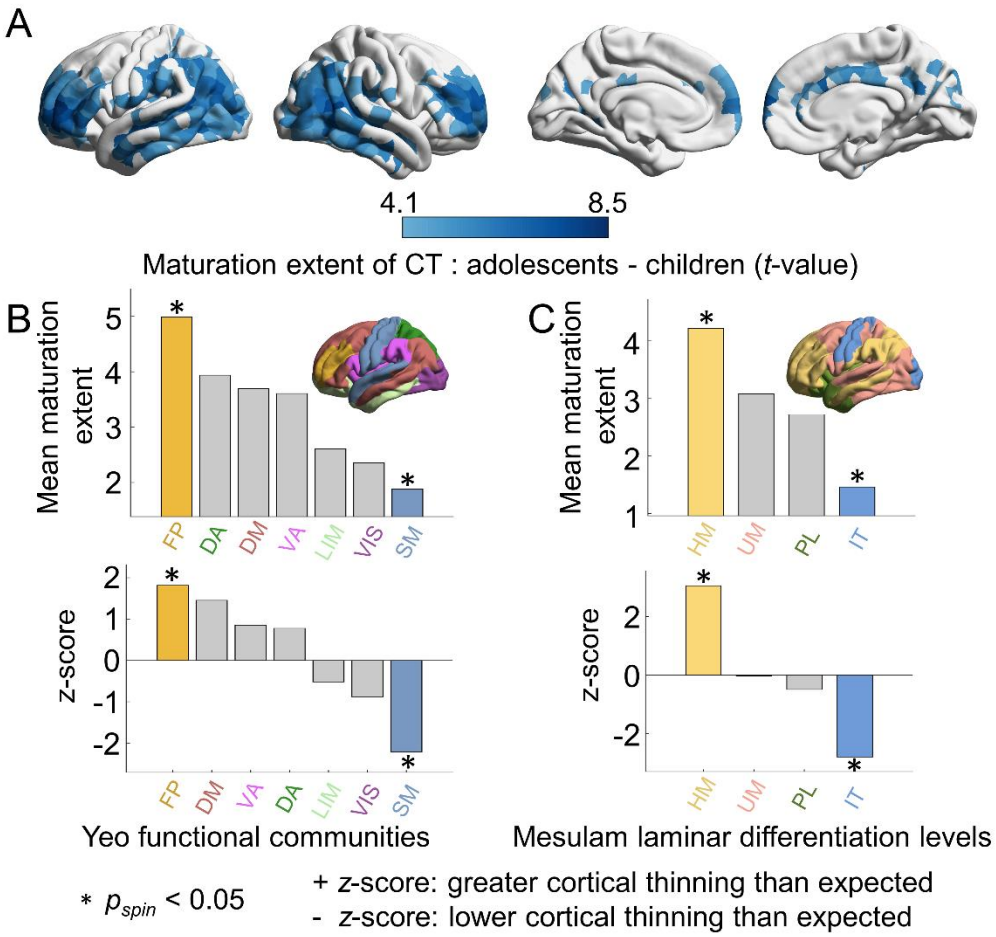

Figure 1. CT maturation from childhood to adolescence. (**A**) Spatial maturation map of CT from childhood to adolescence. A greater positive *t*-value denotes more pronounced cortical thinning with development. The maps were corrected using a Bonferroni correction method for multiple comparisons ($p_{bonf} < 0.05$). (**B**) The mean CT maturation extent (estimated by *t*-value) within each brain community was defined by Yeo et al. (34), and the laminar differentiation level was defined by Mesulam et al. (37) (**C**). Spin tests (35, 36) were performed by spherical projection and rotation class positions 1000 times for correcting spatial autocorrelations, and the class-specific mean *t*-values were expressed as *z* scores relative to this null model. A positive *z* score indicated higher cortical thinning than expected by chance. Asterisks denote statistical significance ($p_{spin} < 0.05$). VIS, visual; SM, somatomotor; LIM, limbic; DA, dorsal attention; VA, ventral attention; FP, frontoparietal; DM, default mode; IT, idiotypic; PL, paralimbic; UM, unimodal and HM, heteromodal. Values of a brain map were visualized using BrainNet Viewer (87).

bioRxiv preprint doi: https://doi.org/10.1101/2022.12.15.520527; this version posted December 15, 2022. The copyright holder for this preprint (which was not certified by peer review) is the author/funder, who has granted bioRxiv a license to display the preprint in perpetuity. It is made available under aCC-BY-NC-ND 4.0 International license.

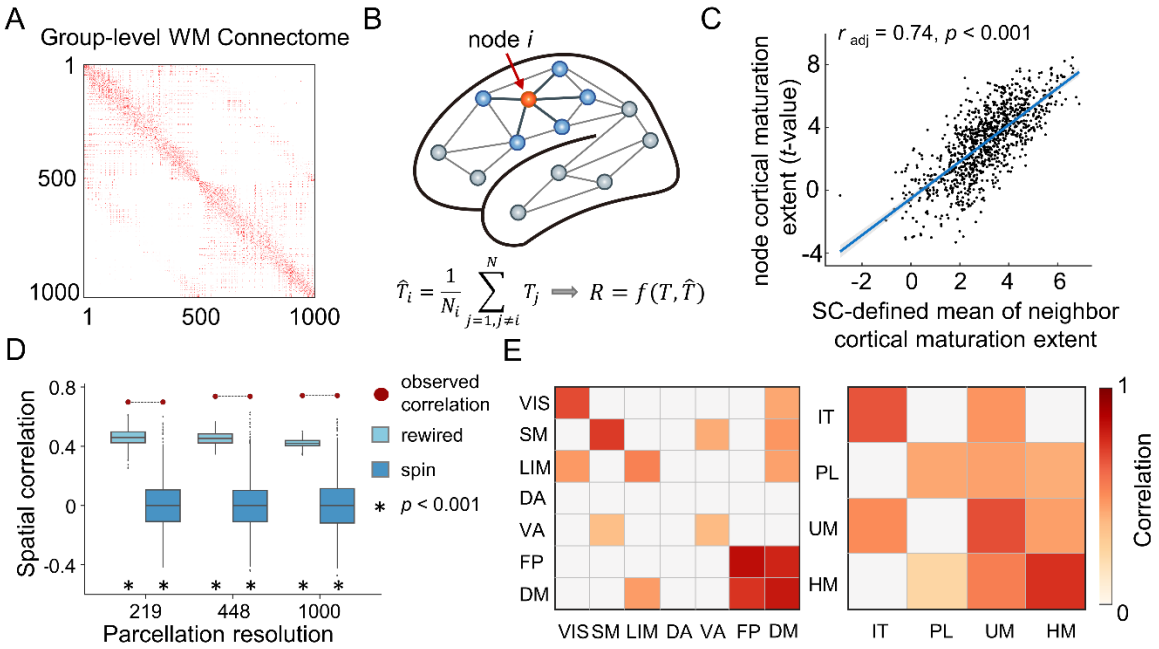

Figure 2. WM network-based CT maturation. (**A**) Group-level connectome backbone at 1000-node resolution. (**B**) Schematic diagram of WM network-constrained CT maturation. The CT maturation extent of a given node (orange) was correlated with the mean maturation extent of its directly connected neighbors (blue) to test whether the maturation of CT is shaped by the underlying WM network architecture. (**C**) A significant correlation was observed between the nodal CT maturation extent and the mean of its directly connected neighbors (r_{adj} = 0.74, P = 5.56×10^{-176}). The scatter plot shows the result at 1000-node resolution. See *SI Appendix*, Fig. S3 for results at other resolutions. (**D**) The observed correlations across 3 resolutions (shown as red circles) were compared against two baseline null models. (1) To determine whether these correlations were driven by the basic spatial embedding of the WM network, we randomly rewired edges while preserving the nodal degree and edge length distribution of the empirical WM network ("rewired", 1000 times, shown as light blue boxes). (2) To determine whether these correlations were driven by spatial autocorrelation, we generated 1000 surrogate maps by rotating region-level cortical t values ("spin test", shown as deep blue boxes). Asterisks denote statistical significance (p < 0.001). (**E**) The spatial correlation at the system level. The whole-brain cortical nodes were classified into seven classic communities (34) (left) and four laminar differentiation levels (37) (right), and the statistically significant (p_{spin} < 0.05, FDR corrected) correlations are shown in color. VIS, visual; SM, somatomotor; LIM, limbic; DA, dorsal attention; VA, ventral attention; FP, frontoparietal; DM, default mode; IT, idiotypic; PL, paralimbic; UM, unimodal and HM, heteromodal.

bioRxiv preprint doi: https://doi.org/10.1101/2022.12.15.520527; this version posted December 15, 2022. The copyright holder for this preprint (which was not certified by peer review) is the author/funder, who has granted bioRxiv a license to display the preprint in perpetuity. It is made available under aCC-BY-NC-ND 4.0 International license.

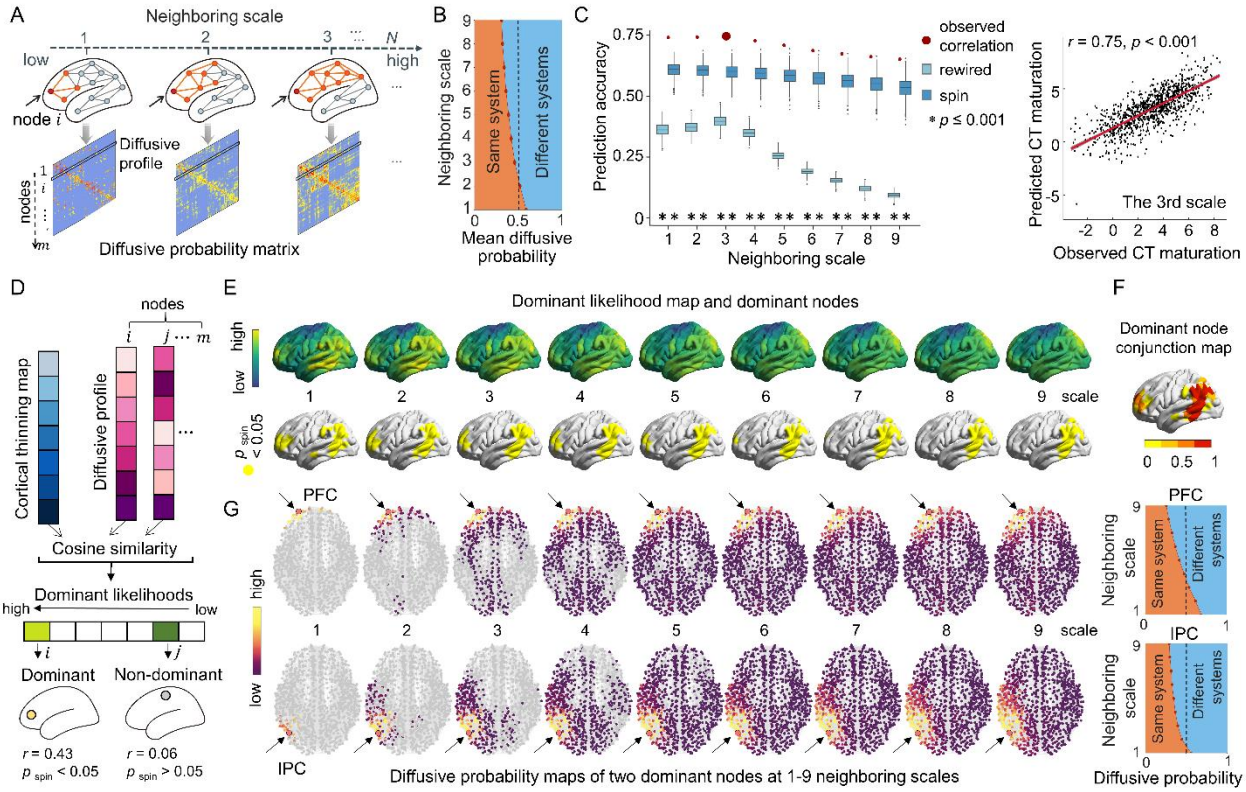

Figure 3. Network-based diffusion model. (**A**) Schematic diagram of nodal diffusion processes through multiscale WM edge paths. The orange color represents the edges and nodes at the *nth* neighboring scale of a given node *i* (red). For the first neighboring scale, the diffusion probabilities of node *i* to its neighbors during one random walk step are $1/d_i$, where d_i is the node degree of *i*. As the moving steps increase, the scale of the probed neighbor nodes also expands and the diffusion probabilities to each neighbor are recalculated iteratively. The diffusive profiles of all nodes form the diffusive probability matrix at each neighboring scale. (**B**) The curve of the average diffusive probability of whole-brain nodes within the same cortical system and between systems. It illustrates that the diffusion probability within the same cortical system was greater than 0.5 at the first scale and then decreases with the expansion of neighboring scales. (**C**) Significant correlations between the predicted CT maturation and the observed CT maturation. The observed correlations (red dots) were compared to the correlations obtained from 1000 rewired tests (light blue boxes) and 1000 spin tests (deep blue boxes). Asterisks denote statistical significance ($p <= 0.001$). The box plot shows the result at 1000-node resolution. See *SI Appendix*, Fig. S5 for results at other resolutions. The scatter plot on the right depicts the correlation between actual and predicted CT maturation at the 3rd neighboring scale, which exhibited the highest prediction accuracy, as an example. (**D**) Schematic of dominant brain region identification. Dominators are regions whose diffusion profiles show significant cosine similarity with the CT maturation map. Spin tests (1000 times) were used to evaluate the statistical significance. (**E**) Regional distributions of dominant likelihood (cosine similarity) between nodal diffusion profiles and CT maturation map at 1-9 neighboring scales (top panels) and the spatial distributions of dominant regions ($p_{spin} < 0.05$, bottom panels). *SI Appendix*, Fig. S6A-B and Fig.S7 depict the results in other view directions and in other parcellation resolutions. (**F**) The conjunction map of dominant nodes across all nine neighboring scales shows the

bioRxiv preprint doi: https://doi.org/10.1101/2022.12.15.520527; this version posted December 15, 2022. The copyright holder for this preprint (which was not certified by peer review) is the author/funder, who has granted bioRxiv a license to display the preprint in perpetuity. It is made available under aCC-BY-NC-ND 4.0 International license.

probability of each node being identified as a dominant node across scales. (**G**) The diffusive probability distribution of two representative dominant nodes separately in the prefrontal cortex (PFC, top panels) and inferior parietal cortex (IPC, bottom panels) at each 1-9 neighboring scale. A node with a brighter color represents a greater diffusive probability between that node and the dominant node. The right panels show the diffusive probability of both dominant nodes within the same cortical system and between systems. As the neighborhood scale expands, the diffusion of these two nodes spreads from local communities to nearby and distributed communities across whole brain. These diffusion processes were mainly involved in nodes within system at low neighboring scales while in nodes between systems at high scales.

bioRxiv preprint doi: https://doi.org/10.1101/2022.12.15.520527; this version posted December 15, 2022. The copyright holder for this preprint (which was not certified by peer review) is the author/funder, who has granted bioRxiv a license to display the preprint in perpetuity. It is made available under aCC-BY-NC-ND 4.0 International license.

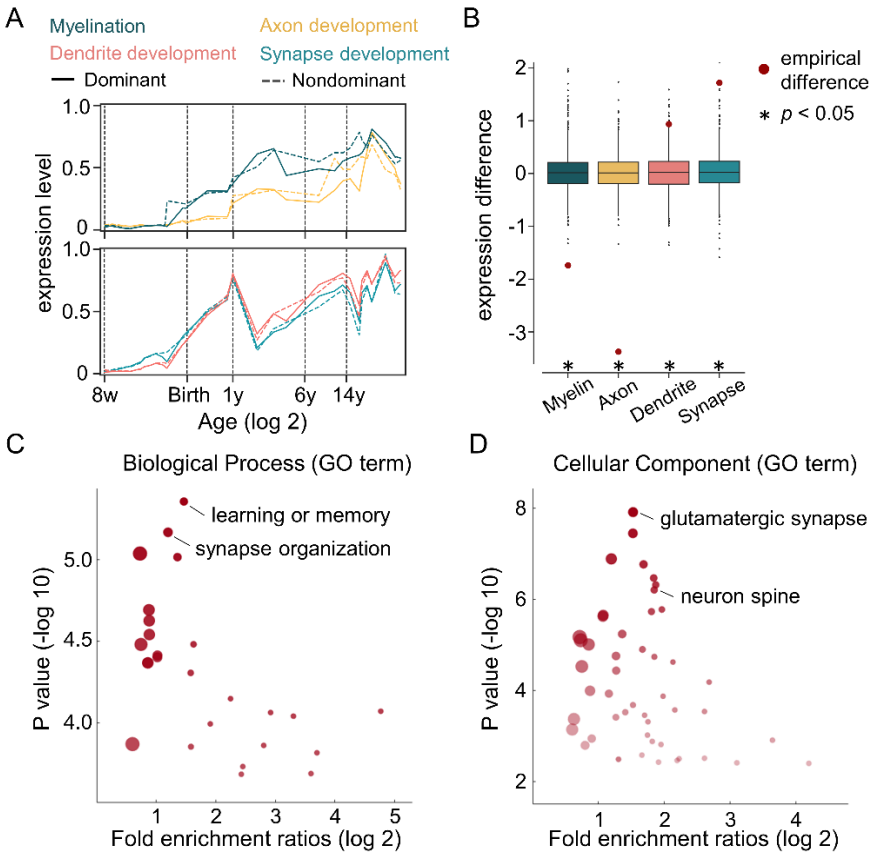

Figure 4. Association between regional heterogeneous constraints and gene expression profiles. (**A**) Transcriptomic trajectories between dominant regions (solid line) and non-dominant regions (dashed line) in four maturation processes. Here, we calculated the first principal component score of each gene set's transcription level. (**B**) Transcriptomic differences between dominant and non-dominant regions from childhood to adolescence. For each maturation process, the statistical significance was calculated by comparing the empirical difference (red dots) against null differences generated by randomly resampling the same number of genes 1000 times from the remaining genes. Asterisks denote statistical significance ($p < 0.05$). (**C**) Volcano plot depicts Gene Ontology (GO) results for Biological Processes and Cellular Components (**D**). The dots represent the GO terms corrected for multiple comparisons (FDR-corrected, $P < 0.05$). The size of the dot indicates the number of genes belonging to the corresponding GO term, and the transparency of the dot represents the significance of the corresponding GO term.

bioRxiv preprint doi: https://doi.org/10.1101/2022.12.15.520527; this version posted December 15, 2022. The copyright holder for this preprint (which was not certified by peer review) is the author/funder, who has granted bioRxiv a license to display the preprint in perpetuity. It is made available under aCC-BY-NC-ND 4.0 International license.

Supporting Information (SI) Appendix for

Structural connectome architecture shapes the maturation of cortical morphology from childhood to adolescence

Xinyuan Liang, Lianglong Sun, Xuhong Liao, Tianyuan Lei, Mingrui Xia, Dingna Duan, Zilong Zeng, Zhilei Xu, Weiwei Men, Yanpei Wang, Shuping Tan, Jia-Hong Gao, Shaozheng Qin, Sha Tao, Qi Dong, Tengda Zhao, Yong He

Corresponding authors:

Yong He, Ph.D., E-mail: yong.he@bnu.edu.cn
Tengda Zhao, Ph.D., E-mail: tengdazhao@bnu.edu.cn

bioRxiv preprint doi: https://doi.org/10.1101/2022.12.15.520527; this version posted December 15, 2022. The copyright holder for this preprint (which was not certified by peer review) is the author/funder, who has granted bioRxiv a license to display the preprint in perpetuity. It is made available under aCC-BY-NC-ND 4.0 International license.

SI-1. Participants and MRI Data Analyses

1.1 Participants

We performed analyses in two independent datasets. The Discovery Dataset included a longitudinal cohort of 358 typically developing participants (aged 6-14 years, 651 scans from 195 males and 163 females) from the Beijing Cohort in Children Brain Development (CBD) project. All the individuals were recruited from primary schools in Beijing. The exclusion criteria included cognitive anomalies (1), significant physical illness or history of neurological/psychiatric disorders, significant head injuries, abuse of illegal drugs and alcohol, or contraindications for MRI. Some of these participants were invited to take part in up to three repeated MRI scans, with an interval of approximately one year between each scan. Informed written consent was obtained from all participants and at least one parent/guardian, consistent with the guidelines of the Ethics Committee of Beijing Normal University.

After strict quality control, a total of 130 scans were excluded. Specifically, 76 scans were excluded due to artifacts in T1-weighted (T1w) images, 39 and 15 scans were excluded due to high in-scanner motion (maximum head motion > 3 mm) and serious signal dropout, respectively in diffusion MRI (dMRI) images. Finally, 521 scans from 314 participants (aged 6-14 years, 153 females) were included in the study. Among these included participants, 158 participants had one scan, 105 participants had two scans, and 51 participants had three scans. According to the criteria from a previous public health investigation (2) and the WHO (3), these participants were then divided into two sex-balanced groups: 299 scans in the child group (6-10 years, mean (± SD) age 8.68 ± 0.94 years, 157 females) and 222 scans in the adolescent group (10-14 years, mean age 11.19 ± 0.94 years, 108 females).

For reproducibility analyses, we also included a cross-sectional Replication Dataset from the Lifespan Human Connectome Project in Development (HCP-D) (4). Participants were recruited across four imaging sites: (1) Harvard University, (2) University of California-Los Angeles, (3) University of Minnesota, and (4) Washington University in St. Louis (WUSTL). Details on the inclusion and exclusion criteria can be found in (4). All procedures were approved by a central Institutional Review Board administered at Washington University in St. Louis (IRB #201603135).

In this Replication Dataset, we initially included 301 typically developing participants aged 5 to 14 (192 females). First, we excluded 3 participants with anatomical anomalies and 17 participants with notable myelin map quality issues according to each subject's quality control report of structural MR images (4). After these, T1w images of 98 children (5-10 years, mean age 8.72 ± 0.99 years, 32 females) and 203 adolescents (10-14 years, mean age 12.17 ± 1.28 years, 86 females) were eventually included. Next, for dMRI images, we excluded 30 participants due to serious signal dropout (based on eddy-corrected dMRI images) and 4 participants due to high in-scanner motion (maximum head motion > 3 mm) in the child group. After these, diffusion images from 64 children were included in this study.

1.2 Image Acquisition

For the Discovery Dataset, high-resolution T1w images for each subject were scanned at Peking University using a 3T Siemens Prisma scanner. T1w images were acquired using the following

bioRxiv preprint doi: https://doi.org/10.1101/2022.12.15.520527; this version posted December 15, 2022. The copyright holder for this preprint (which was not certified by peer review) is the author/funder, who has granted bioRxiv a license to display the preprint in perpetuity. It is made available under aCC-BY-NC-ND 4.0 International license.

parameters: repetition time (TR) = 2530 ms, echo time (TE) = 2.98 ms, inversion time (TI) = 1100 ms, flip angle (FA) =7°, acquisition matrix = 256×224, field of view (FOV) = 256×224 mm^2, slice number = 192, slice thickness = 1 mm, bandwidth (BW) = 240 Hz/Px. Diffusion-weighted images were acquired using the high angular resolution diffusion imaging (HARDI) sequence with a 64-channel head coil with parameters as follows: TR = 7500 ms, TE = 64 ms, acquisition matrix = 112×112, FOV = 224×224 mm^2, slices = 70, slice thickness = 2 mm, BW = 2030 Hz/Px, 64 diffusion weighted directions (b-value = 1000 s/mm^2) with 10 non-diffusion weighted b0 (0 s/mm^2).

For the Replication Dataset, high-resolution T1w images were scanned on a 3T Siemens Prisma using the following parameters (5): TR = 2500 ms, TE = 1.8/3.6/5.4/7.2 ms, TI = 1000 ms, FA = 8°, slice thickness = 0.8 mm, and in-plane acceleration factor = 2. Parameters for diffusion MRI were as follows: TR = 3230 ms, TE = 89 ms, slice thickness = 1.5 mm, multiband acceleration factor = 4, 92-93 directions per shell (b = 1500/3000 mm^2). There are 28 b0 volumes equally interspersed across four consecutive dMRI runs. Therefore, each individual acquired two images with 199 volumes in the opposite phase encoding direction (AP and PA).

1.3 MRI Data Preprocessing

For the Discovery Dataset, cortical reconstruction was performed using FreeSurfer v6.0 image analysis suite (https://surfer.nmr.mgh.harvard.edu/). This processing includes intensity normalization, nonbrain tissue removal, tissue segmentation, automated cortical reconstruction, and surface parcellation (6-10). To improve the quality of nonbrain tissue removal, we used HD-BET (11), an artificial neural network-based tool, to automatically extract brain tissue images that were further used to replace the *brainmask.mgz* files in FreeSurfer for subsequent processing. To reconstruct the individual cortical surface, all images were first processed cross-sectionally and then processed through the longitudinal stream (12, 13) in FreeSurfer to obtain more sensitive and reliable measurements of cortical morphology. Specifically, an unbiased within-subject template based on all available time points was created for each individual with longitudinal scans. This template was used to provide initial information for segmentation and cortical reconstruction to reduce random variation during nonlinear optimization within each subject. Next, we constructed a custom registration template by averaging all available subjects' cortical surfaces. The atlas in the standard *fsaverage* space was registered to the new custom template and then registered to each subject's surface space to be used to obtain regional cortical thickness (CT) measurements. All images were visually inspected and manually edited and corrected where needed by a trained researcher (X.Y.L.) to ensure the correctness of gray matter (GM) and white matter (WM) boundaries and improve the quality of the output. Diffusion data were first denoised, and Gibbs ringing artifacts (14) were removed using MRtrix 3.0 (15). Next, we corrected eddy current-induced distortions, head movements, and signal dropout using the FSL eddy tool (16-18). Then, we fed the eddy-corrected DW images and corresponding fieldmap images into the FSL epi_reg script (https://fsl.fmrib.ox.ac.uk/fsl/fslwiki/FLIRT/UserGuide#epi_reg) to remove EPI susceptibility artifacts. Finally, B1 field inhomogeneity was corrected for the dMRI images with the N4 algorithm available in ANTS (19).

For the Replication Dataset, the T1w data went through the HCP preprocessing pipeline (20). We obtained the individual CT in a common 32k_fs_LR space from the publicly available dataset. Diffusion data were first denoised, and Gibbs ringing artifacts were removed. Then, we used topup/eddy (16-18, 21) to correct the EPI distortions, eddy currents, subject movement

bioRxiv preprint doi: https://doi.org/10.1101/2022.12.15.520527; this version posted December 15, 2022. The copyright holder for this preprint (which was not certified by peer review) is the author/funder, who has granted bioRxiv a license to display the preprint in perpetuity. It is made available under aCC-BY-NC-ND 4.0 International license.

distortions, and signal dropout. Finally, B1 field inhomogeneity was corrected for the dMRI images.

1.4 Analysis of CT from Childhood to Adolescence

First, we employed an anatomical brain atlas with multi-scale regional parcels (22) based on the classical Desikan-Kiliany parcellation (10, 23) to divide each participant's cortical surface into 1000 approximately equally sized regions of interest (ROIs). To evaluate the impact of nodal resolution, we also parcellated the cortical surface into 219 and 448 nodes, respectively. The CT of each brain node was estimated by calculating the average thickness of all vertices in that nodal ROI.

To estimate the nodal maturation map of whole brain CT from childhood to adolescence in the Discovery Dataset, we applied a mixed linear model analysis for each brain node (24). The linear model included the group as the fixed variable of interest, sex as the fixed effect covariates, and the subject-specific intercept as the random effect and was defined as follows:

$$CT_{ij} = \beta_0 + b_i + (\beta_{group} + b_{group,i}) \cdot group_{ij} + \beta_{sex} \cdot sex_i + \varepsilon_{ij}$$

Specifically, CT_{ij} is the CT of participant i at the jth scan, β_{group} represents the fixed group effect of participant *i*, $b_{group,i}$ is the random effect, and ε_{ij} is the residual. The *T* statistics obtained from the group term were used to represent the maturation extent of CT from childhood to adolescence. Greater positive values of *T* indicated more significant cortical thinning.

For the multicentric cross-sectional Replication Dataset, the maturation extent of CT was modeled as follows:

$$CT_{is} = \beta_0 + b_i + (\beta_{group} + b_{group,i}) \cdot group_{is} + \beta_{sex} \cdot sex_i + \varepsilon_{is}$$

where CT_{is} is the cortical thickness of participant i at the sth site.

SI-2. Estimating the Maturation Pattern of CT and Its Associations with WM Connectome Structure from Childhood to Adolescence

2.1 WM Connectome Construction

We reconstructed anatomical streamlines between each two cortical regions based on diffusion MR images to generate the cortical WM network. This procedure was constructed using DSI Studio software (https://www. nitrc.org/projects/dsistudio). First, an SRC file was generated from the dMRI image for each child. Then, we generated spin distribution function (SDF) maps using the generalized q-sampling imaging (GQI) algorithm (25) with a diffusion sampling length ratio of 1.25. The GQI is a model-free method to estimate the anisotropy of diffusing water, which is suitable for reconstructing crossing fibers (26). Deterministic fiber tracking (27) was performed in the individual native dMRI space according to the following steps. We first generated the gray-white boundary mask by dilating the GM atlas 2 voxels toward the inner boundaries and taking the intersection of the WM mask. Then, we merged the original GM atlas and the GM-WM boundary to obtain a seed mask. Next, we defined the terminative mask as

bioRxiv preprint doi: https://doi.org/10.1101/2022.12.15.520527; this version posted December 15, 2022. The copyright holder for this preprint (which was not certified by peer review) is the author/funder, who has granted bioRxiv a license to display the preprint in perpetuity. It is made available under aCC-BY-NC-ND 4.0 International license.

cerebrospinal fluid (CSF) and subcortical regions. All these masks were transformed from the native T1w space into the native dMRI space using the individual mean b0 image as the co-registered target in ANTS (19). Last, ten million streamlines were generated with a step size of 0.625 mm. The anisotropy threshold was set as default, and the turning angle threshold was 45°. Streamlines smaller than 6 mm or larger than 250 mm were further removed. For each child, the connectivity matrices weighted by fiber density (defined as the fiber number normalized by the mean surface area of the two brain regions) were generated using the same parcellations as described above. Finally, the binary group-level WM backbones were created using a consensus approach that preserves the connection length distributions of individual children (28).

2.2 Association between CT Maturation and WM Connectome Structure

We first estimated the constraints of the whole brain WM network on the maturation of nodal CT followed by the method introduced by Shafiei et al. (29). Specifically, we used the group-level binary WM network to define the WM-connected neighbors of each cortical node. Next, we assessed the across-node relationship between the CT maturation extent (*t*-value between child and adolescent groups) of a node and its directly connected neighbor nodes by a model as follows:

$$\hat{T}_i = \frac{1}{N_i} \sum_{j \neq i, j=1}^{N_i} T_j$$

In this model, $\hat{T}_i$ represents the predicted CT maturation extent of node i according to its directly connected neighbors. T_j represents the CT maturation extent (t values as mentioned above) of the *jth* neighbor, and N_i is the number of directly connected neighbors of node i. Then, we calculated the spatial correlation between the empirical CT maturation extent (nodal *t*-value) and the predicted values ($\hat{T}_i$). The correlation coefficient was used to represent the constraint degree between the WM edges and the nodal maturation pattern of CT. To further estimate the spatial constraints at the system level, we classified the whole-brain cortical nodes into 7 classic communities (30). Next, we calculated the constraint degree across nodes in each sub-network within system and between systems (only when there are more than 10 connections between any two systems). We also repeated the analyses by classifying the brain nodes into 4 laminar differentiation levels (31).

2.3 Null Models of Spatial Correlations

We further tested the observed spatial correlation against two baseline null models. In the first null model, we used a spatial permutation test ("spin test") to explore whether the observed correlation is specific to the actual CT maturation pattern rather than the spatial autocorrelation of CT maturation (32, 33). Specifically, we first record the spherical coordinates of centroids for each parcel in the Cammoun atlas (23). Then, we randomly rotated the parcels while maintaining spatial autocorrelation and reassigned node values to the nearest parcels. This procedure was repeated 1000 times to create surrogate *t*-maps. The *p*-value was calculated as the fraction of correlations in null models exceeding the observed correlation.

In the second null model, we evaluate whether the observed correlation is determined by the

bioRxiv preprint doi: https://doi.org/10.1101/2022.12.15.520527; this version posted December 15, 2022. The copyright holder for this preprint (which was not certified by peer review) is the author/funder, who has granted bioRxiv a license to display the preprint in perpetuity. It is made available under aCC-BY-NC-ND 4.0 International license.

empirical WM network topology rather than the basic spatial embedding of the WM network (such as the distribution of node degree and edge length), we used a rewired null model ("rewired") (34). Specifically, we first divided edges into different bins according to their Euclidean distance. To preserve the degree sequence and approximate edge length distribution of the empirical WM network, edge pairs were randomly swapped within each bin. Finally, 1000 surrogate networks were generated by repeating this procedure. The *p*-value was calculated as the fraction of correlations in null models exceeding the observed correlation.

2.4 Network-based Diffusion Model of WM Connectome to Predict Nodal Morphology Maturation

To further understand the mechanisms of how the maturation process of cortical morphology is constrained by the structural connectome, we present a network-based diffusion model in which the cortical diffusion processes through multiscale WM edge paths could simulate the maturation of nodal CT. Specifically, we combined the random walk model and support vector regression (SVR) to predict CT maturation by employing nodal diffusive profiles at multiple neighboring scales as features. To characterize the multiscale diffusion properties of the WM network at the nodal level, we used the random walk (35) model to simulate the diffusion process between any two brain regions. Specifically, for an adjacency matrix A, if its element A_{ij} is 1, it indicates that there are edges (anatomical connections) between node i and node j, and it is 0 when there is no edge. The probability of node i transferring to its neighbor j during one step is A_{ij}/d_i (modeled by a random walker moving one step along the edges of the WM network), where d_i is the structurally connected neighbor number (node degree) of node i. Thus, the transition probabilities of the WM network were represented by the transition matrix P. P was defined as:

$$\mathbf{P} = \boldsymbol{D}^{-1}\mathbf{A}$$

where $\boldsymbol{D}$ is the node degree diagonal matrix. The initial distribution of random walkers is represented in $\boldsymbol{p}_0$, where the diagonal elements are 1 and the other values are equal to 0. Therefore, when these random walkers move *n* steps (n = 1, 2, 3, …), their distribution can be described as:

$$\mathbf{P}(\mathrm{n}) = \boldsymbol{p}_0\boldsymbol{P}^n$$

The sum of elements in each row of the distribution matrix is 1, reflecting the diffusion preference of each node with its *nth*-order neighborhoods. The maximum number of steps N was set as the diameter of the WM network (the max shortest path length between any pair of nodes). Finally, we averaged the outgoing and incoming random walker distribution matrix as a symmetrical diffusion connectivity matrix at each step to represent the bidirectional diffusion properties between any two nodes. Each row of this matrix represents the diffusive profile at the *nth* neighboring scale of each cortical node. Increasing moving steps present expansion scales of the probed neighborhood, which indicates local to distributed preferences of information exchange during diffusion propagation.

Next, we trained a support vector regression (SVR) model with diffusive profiles at all neighboring scales of a brain node as input features to predict its nodal CT maturation extent. This model was trained in a tenfold cross-validation strategy with a linear kernel. The coefficient of training error, that is, the C parameter, was selected from among 16 values [2^{-5},2^{-4}, …,2^{9}, 2^{10}]

bioRxiv preprint doi: https://doi.org/10.1101/2022.12.15.520527; this version posted December 15, 2022. The copyright holder for this preprint (which was not certified by peer review) is the author/funder, who has granted bioRxiv a license to display the preprint in perpetuity. It is made available under aCC-BY-NC-ND 4.0 International license.

as in a previous study (36). The Pearson correlation coefficient between the empirical and predicted CT maturation extents was calculated as the prediction accuracy. To evaluate the contribution of each scale, we also use the diffusive profiles at each neighboring scale as the input features to further verify the results. Two null models were used to evaluate the significance of prediction accuracy. In the first model, we created 1000 surrogate CT maps by randomly permuting cortical labels while preserving spatial autocorrelation to retrain the SVR models ("spin test"). In the second model, we generated 1000 degree- and edge length-preserving surrogate networks and recalculated diffusion connectivity matrices to retain the SVR models ("rewired", see Null Models). These analyses were performed using the LIBSVM toolbox (https://www.csie.ntu.edu.tw/~cjlin/ libsvm/).

2.5 Identifying the Dominant Regions during Development

Dominant regions during development were identified by calculating the cosine similarity between the CT maturation map and the diffusion profiles at each random walk step. The high similarity of a node indicates that its neighboring diffusion preference more spatially resembled its neighboring distribution of CT maturation, suggesting a more important role in leading cortical development. The statistical significance of the spatial similarity for each brain region was assessed by using a spatial permutation test (1000 times, see Null Models). Regions with significantly greater spatial similarity ($p_{spin} < 0.05$) were identified as the dominant regions during development.

We further replicated our results using the other method introduced by (29), which aims to find some brain regions that show high maturation extents in both themselves and their directly connected neighbors. To identify such regions, we ranked the nodes' CT maturation extents and their neighbors' mean CT maturation extents in ascending order. For each node, we calculated the mean rank across both lists. The significance of rankings was evaluated using the spin test (1000 times, see Null Models). Regions with significantly higher ranks ($p_{spin} < 0.05$) were identified as the dominant regions.

SI-3. Relationship between Heterogeneous Connectome Constraints on Cortical Maturation and Gene Expression Profiles

3.1 BrainSpan Atlas

The BrainSpan data (37) provided developmental gene expression in brain tissue samples from 8 postconception weeks to 40 years. The 42 donors were divided into five groups based on their age, including fetal (8-37 postconception weeks), infant (4 months-1 year), child (2-8 years), adolescent (11-19 years), and adult (21-40 years). Only neocortical regions were included in our study. There were four tissue samples excluded (primary motor-sensory cortex (samples), occipital neocortex, parietal neocortex, temporal neocortex) with gene expression values only in the early fetal period (38). Genes with 0 expression values in all tissue samples were removed. Then, we divided these samples into dominant and non-dominant categories according to their anatomical location (from 11 areas of the neocortex) and arranged them in ascending order based on age to explore the temporal characteristics of gene expression. Next, we selected four gene sets (39) that cover typical maturation procedures involved in both CT and WM, including axon development, myelination, dendrite development, and synapse development, to evaluate whether

bioRxiv preprint doi: https://doi.org/10.1101/2022.12.15.520527; this version posted December 15, 2022. The copyright holder for this preprint (which was not certified by peer review) is the author/funder, who has granted bioRxiv a license to display the preprint in perpetuity. It is made available under aCC-BY-NC-ND 4.0 International license.

there are differences in transcription levels between dominant and non-dominant regions. For each gene set, we performed principal component analysis (PCA) on the gene expression matrix to calculate the first principal component score of each gene set's transcription level in dominant and non-dominant regions. The transcriptomic trajectories were characterized by using locally weighted regression to fit the first principal component score with the postconceptional days (log2) as in a previous study (39). For visualization, we scaled the first principal component score to the range 0-1 across all tissue samples using min-max normalization.

To assess the significance of the difference for each gene set, we calculated the difference between the means of the first principal component scores of the two categories of brain regions. Please note that we only include tissue samples within the age range of individuals included in the CBD dataset (6 to 14 years) here. Specifically, there were 16 sample tissues (mean age 10 ± 2.19 years) in dominant regions and 25 sample tissues (mean age 10.24 ± 2.17 years) in non-dominant regions. Of note, these two groups of samples were matched in age distribution (*t* value = -0.34, *P* value = 0.73). Next, we randomly sampled an equal number of genes with each gene set from the remaining genes in BrainSpan datasets and recalculated the difference and compared the observed transcription level differences against the null distributions generated by repeating 1000 permutation tests.

3.2 Allen Human Brain Atlas

The regional gene expression data were obtained from Allen Human Brain Atlas datasets (http://human.brain-map.org) (40). Since only two of the six donors (mean age: 42.50 ± 13.38 years; 1 female) contained whole-brain data, we only considered the left hemisphere here. To obtain the gene transcriptional profile of each brain region, the regional microarray expression data were preprocessed using a recommended pipeline with the abagen toolbox (41, 42). First, probe reannotation was performed according to the information provided by (41). Second, we used the intensity-based method to remove the probes that did not exceed background noise in at least 50% of tissue samples across all donors. When multiple probes can represent the expression of the same gene, we retained the probe with the highest differential stability across donors. The differential stability was defined as:

$$\mathrm{DS}\,(\mathrm{p}) = \frac{1}{\binom{N}{2}} \sum_{i=1}^{N-1} \sum_{j=i+1}^{N} r\left[B_i(p), B_j(p)\right]$$

where N is the number of donors, p is a single probe, and r is the Spearman correlation of microarray expression values across brain regions in donor B_i and donor B_j. Next, the MNI coordinates of the samples were updated to those generated by using nonlinear registration. Under the guidance of MNI coordinates, tissue samples were assigned to the brain regions according to the given atlas by searching the nearest brain region within 2 mm. In this process, hemisphere and gross structural information were also used to reduce the assigning bias. All samples not assigned to a brain region were discarded.

To mitigate the differences in microarray expression between donors, we used a scaled robust sigmoid function to normalize each sample across all genes (43).

bioRxiv preprint doi: https://doi.org/10.1101/2022.12.15.520527; this version posted December 15, 2022. The copyright holder for this preprint (which was not certified by peer review) is the author/funder, who has granted bioRxiv a license to display the preprint in perpetuity. It is made available under aCC-BY-NC-ND 4.0 International license.

$$x_{norm} = \frac{1}{1 + \exp(\frac{-(x_i - \langle x \rangle)}{IQR_x})}$$

where $\langle x \rangle$ represents the median and IQR is the interquartile range. Then, we rescaled the normalized expression values to the unit interval using the min-max function:

$$x_{scaled} = \frac{x_{norm} - \min(x_{norm})}{\max(x_{norm}) - \min(x_{norm})}$$

Each gene expression value was normalized across all samples by using the same method. Tissue samples assigned to the same parcel were averaged separately for each donor and then averaged across six donors. Finally, stable genes with differential stability greater than 0.1 were retained for our analysis (38). Genes with greater differential stability are more consistent across donors and more biologically relevant, such as disease, drug targets, and literature citations (40). After preprocessing, a gene expression matrix (111 brain regions × 8631 gene expression levels) was generated. Then, we identified the association between the dominant likelihood map at the 3rd neighboring scale (which exhibited the highest prediction accuracy) and each gene expression map using Pearson's correlation and spin tests (1000 times).

3.3 Gene Ontology Enrichment Analysis

We performed the Gene Ontology enrichment analysis on gene sets using the ToppGene Suite (44) according to the following thresholds: (1) *P* value cutoff was 10^{-5} in the advanced parameter settings, (2) *q-value* < 0.05 in Benjamini–Hochberg false discovery rate (FDR) corrections. The significant enrichment terms for both positively correlated and negatively correlated gene sets are shown in S7-S8. We used the online tool REViGO (http://revigo.irb.hr) to select the most meaningful GO terms and highlight them.

bioRxiv preprint doi: https://doi.org/10.1101/2022.12.15.520527; this version posted December 15, 2022. The copyright holder for this preprint (which was not certified by peer review) is the author/funder, who has granted bioRxiv a license to display the preprint in perpetuity. It is made available under aCC-BY-NC-ND 4.0 International license.

References

1. Q. Dong, C. Lin (2011) Standardized tests of the National Children's Study of China. (Beijing: Science Press).
2. S. M. Sawyer, P. S. Azzopardi, D. Wickremarathne, G. C. Patton, The age of adolescence. *The Lancet Child & Adolescent Health* **2**, 223-228 (2018).
3. J. A. Singh, M. Siddiqi, P. Parameshwar, V. Chandra-Mouli, World Health Organization guidance on ethical considerations in planning and reviewing research studies on sexual and reproductive health in adolescents. *Journal of Adolescent Health* **64**, 427-429 (2019).
4. L. H. Somerville *et al.*, The Lifespan Human Connectome Project in Development: A large-scale study of brain connectivity development in 5-21 year olds. *Neuroimage* **183**, 456-468 (2018).
5. M. P. Harms *et al.*, Extending the Human Connectome Project across ages: Imaging protocols for the Lifespan Development and Aging projects. *Neuroimage* **183**, 972-984 (2018).
6. B. Fischl, A. M. Dale, Measuring the thickness of the human cerebral cortex from magnetic resonance images. *Proceedings of the National Academy of Sciences* **97**, 11050-11055 (2000).
7. B. Fischl, M. I. Sereno, A. M. Dale, Cortical surface-based analysis: II: inflation, flattening, and a surface-based coordinate system. *Neuroimage* **9**, 195-207 (1999).
8. A. M. Dale, B. Fischl, M. I. Sereno, Cortical surface-based analysis: I. Segmentation and surface reconstruction. *Neuroimage* **9**, 179-194 (1999).
9. B. Fischl *et al.*, Automatically parcellating the human cerebral cortex. *Cerebral cortex* **14**, 11-22 (2004).
10. R. S. Desikan *et al.*, An automated labeling system for subdividing the human cerebral cortex on MRI scans into gyral based regions of interest. *Neuroimage* **31**, 968-980 (2006).
11. F. Isensee *et al.*, Automated brain extraction of multisequence MRI using artificial neural networks. *Hum Brain Mapp* **40**, 4952-4964 (2019).
12. M. Reuter, N. J. Schmansky, H. D. Rosas, B. Fischl, Within-subject template estimation for unbiased longitudinal image analysis. *Neuroimage* **61**, 1402-1418 (2012).
13. M. Reuter, H. D. Rosas, B. Fischl, Highly accurate inverse consistent registration: a robust approach. *Neuroimage* **53**, 1181-1196 (2010).
14. E. Kellner, B. Dhital, V. G. Kiselev, M. Reisert, Gibbs-ringing artifact removal based on local subvoxel-shifts. *Magnetic resonance in medicine* **76**, 1574-1581 (2016).
15. J. D. Tournier *et al.*, MRtrix3: A fast, flexible and open software framework for medical image processing and visualisation. *Neuroimage* **202**, 116137 (2019).
16. J. L. Andersson, S. N. Sotiropoulos, An integrated approach to correction for off-resonance effects and subject movement in diffusion MR imaging. *Neuroimage* **125**, 1063-1078 (2016).
17. J. L. Andersson *et al.*, Towards a comprehensive framework for movement and distortion correction of diffusion MR images: Within volume movement. *Neuroimage* **152**, 450-466 (2017).
18. J. L. Andersson, M. S. Graham, E. Zsoldos, S. N. Sotiropoulos, Incorporating outlier detection and replacement into a non-parametric framework for movement and distortion correction of diffusion MR images. *Neuroimage* **141**, 556-572 (2016).
19. N. J. Tustison *et al.*, N4ITK: improved N3 bias correction. *IEEE transactions on medical*

bioRxiv preprint doi: https://doi.org/10.1101/2022.12.15.520527; this version posted December 15, 2022. The copyright holder for this preprint (which was not certified by peer review) is the author/funder, who has granted bioRxiv a license to display the preprint in perpetuity. It is made available under aCC-BY-NC-ND 4.0 International license.

imaging **29**, 1310-1320 (2010).
20. M. F. Glasser *et al.*, The minimal preprocessing pipelines for the Human Connectome Project. *Neuroimage* **80**, 105-124 (2013).
21. J. L. Andersson, S. Skare, J. Ashburner, How to correct susceptibility distortions in spin-echo echo-planar images: application to diffusion tensor imaging. *Neuroimage* **20**, 870-888 (2003).
22. A. Zalesky *et al.*, Whole-brain anatomical networks: does the choice of nodes matter? *Neuroimage* **50**, 970-983 (2010).
23. L. Cammoun *et al.*, Mapping the human connectome at multiple scales with diffusion spectrum MRI. *Journal of neuroscience methods* **203**, 386-397 (2012).
24. N. M. Laird, J. H. Ware, Random-effects models for longitudinal data. *Biometrics*, 963-974 (1982).
25. F.-C. Yeh, V. J. Wedeen, W.-Y. I. Tseng, Generalized *q*-sampling imaging. *IEEE transactions on medical imaging* **29**, 1626-1635 (2010).
26. Z. Jin *et al.*, Differences between generalized Q-sampling imaging and diffusion tensor imaging in visualization of crossing neural fibers in the brain. *Surg Radiol Anat* **41**, 1019-1028 (2019).
27. F.-C. Yeh, T. D. Verstynen, Y. Wang, J. C. Fernández-Miranda, W.-Y. I. Tseng, Deterministic diffusion fiber tracking improved by quantitative anisotropy. *PloS one* **8**, e80713 (2013).
28. R. F. Betzel, A. Griffa, P. Hagmann, B. Mišić, Distance-dependent consensus thresholds for generating group-representative structural brain networks. *Network neuroscience* **3**, 475-496 (2019).
29. G. Shafiei *et al.*, Spatial patterning of tissue volume loss in schizophrenia reflects brain network architecture. *Biological psychiatry* **87**, 727-735 (2020).
30. B. T. Yeo *et al.*, The organization of the human cerebral cortex estimated by intrinsic functional connectivity. *Journal of neurophysiology* (2011).
31. M.-M. Mesulam, Behavioral neuroanatomy. *Principles of behavioral and cognitive neurology* **2**, 1-120 (2000).
32. A. F. Alexander-Bloch *et al.*, On testing for spatial correspondence between maps of human brain structure and function. *Neuroimage* **178**, 540-551 (2018).
33. F. Vasa *et al.*, Adolescent Tuning of Association Cortex in Human Structural Brain Networks. *Cereb Cortex* **28**, 281-294 (2018).
34. R. F. Betzel, D. S. Bassett, Specificity and robustness of long-distance connections in weighted, interareal connectomes. *Proceedings of the National Academy of Sciences* **115**, E4880-E4889 (2018).
35. K. Pearson, The problem of the random walk. *Nature* **72**, 294-294 (1905).
36. Z. Cui, G. Gong, The effect of machine learning regression algorithms and sample size on individualized behavioral prediction with functional connectivity features. *Neuroimage* **178**, 622-637 (2018).
37. J. A. Miller *et al.*, Transcriptional landscape of the prenatal human brain. *Nature* **508**, 199-206 (2014).
38. J. Y. Hansen *et al.*, Mapping gene transcription and neurocognition across human neocortex. *Nat Hum Behav* **5**, 1240-1250 (2021).
39. H. J. Kang *et al.*, Spatio-temporal transcriptome of the human brain. *Nature* **478**, 483-489 (2011).

bioRxiv preprint doi: https://doi.org/10.1101/2022.12.15.520527; this version posted December 15, 2022. The copyright holder for this preprint (which was not certified by peer review) is the author/funder, who has granted bioRxiv a license to display the preprint in perpetuity. It is made available under aCC-BY-NC-ND 4.0 International license.

40. M. J. Hawrylycz *et al.*, An anatomically comprehensive atlas of the adult human brain transcriptome. *Nature* **489**, 391-399 (2012).
41. A. Arnatkevičiūtė, B. D. Fulcher, A. Fornito, A practical guide to linking brain-wide gene expression and neuroimaging data. *Neuroimage* **189**, 353-367 (2019).
42. R. D. Markello *et al.*, Standardizing workflows in imaging transcriptomics with the abagen toolbox. *Elife* **10**, e72129 (2021).
43. B. D. Fulcher, A. Fornito, A transcriptional signature of hub connectivity in the mouse connectome. *Proceedings of the National Academy of Sciences* **113**, 1435-1440 (2016).
44. J. Chen, E. E. Bardes, B. J. Aronow, A. G. Jegga, ToppGene Suite for gene list enrichment analysis and candidate gene prioritization. *Nucleic acids research* **37**, W305-W311 (2009).

bioRxiv preprint doi: https://doi.org/10.1101/2022.12.15.520527; this version posted December 15, 2022. The copyright holder for this preprint (which was not certified by peer review) is the author/funder, who has granted bioRxiv a license to display the preprint in perpetuity. It is made available under aCC-BY-NC-ND 4.0 International license.

Table S1 Accuracy to predict the spatial maturation of CT by using multiscale diffusion profiles of network links as features (1000-node resolution).

Neighboring scale	Accuracy	$p_{rewired}$	p_{spin}
1	0.74	<0.001	<0.001
2	0.74	<0.001	<0.001
3	0.75	<0.001	<0.001
4	0.73	<0.001	<0.001
5	0.71	<0.001	<0.001
6	0.69	<0.001	0.001
7	0.67	<0.001	0.001
8	0.66	<0.001	0.001
9	0.65	<0.001	0.001

Note: The table above gives the prediction accuracies and *p*-values (calculated as the fraction of null values exceeding the observed accuracy in the "rewired" test and "spin" test) by using an SVR model with multiscale diffusion profiles of WM network links as features to predict the spatial maturation of CT. Spatial maturation of CT and diffusion profiles of WM network links were obtained from CBD dataset.

bioRxiv preprint doi: https://doi.org/10.1101/2022.12.15.520527; this version posted December 15, 2022. The copyright holder for this preprint (which was not certified by peer review) is the author/funder, who has granted bioRxiv a license to display the preprint in perpetuity. It is made available under aCC-BY-NC-ND 4.0 International license.

Table S2 Accuracy to predict the spatial maturation of CT by using multiscale diffusion profiles of network links as features (219-node resolution).

Neighboring scale	Accuracy	$p_{rewired}$	p_{spin}
1	0.64	<0.001	0.001
2	0.64	<0.001	0.001
3	0.65	<0.001	<0.001
4	0.61	<0.001	0.001
5	0.60	<0.001	<0.001
6	0.56	<0.001	0.001

Note: The table above gives the prediction accuracies and *p*-values (calculated as the fraction of null values exceeding the observed accuracy in the "rewired" test and "spin" test) by using an SVR model with multiscale diffusion profiles of WM network links as features to predict the spatial maturation of CT. Spatial maturation of CT and diffusion profiles of WM network links were obtained from CBD dataset.

bioRxiv preprint doi: https://doi.org/10.1101/2022.12.15.520527; this version posted December 15, 2022. The copyright holder for this preprint (which was not certified by peer review) is the author/funder, who has granted bioRxiv a license to display the preprint in perpetuity. It is made available under aCC-BY-NC-ND 4.0 International license.

Table S3 Accuracy to predict the spatial maturation of CT by using multiscale diffusion profiles of network links as features (448-node resolution).

Neighboring scale	Accuracy	$p_{rewired}$	p_{spin}
1	0.72	<0.001	<0.001
2	0.73	<0.001	<0.001
3	0.73	<0.001	<0.001
4	0.72	<0.001	<0.001
5	0.69	<0.001	<0.001
6	0.68	<0.001	<0.001
7	0.68	<0.001	<0.001

Note: The table above gives the prediction accuracies and *p*-values (calculated as the fraction of null values exceeding the observed accuracy in the "rewired" test and "spin" test) by using an SVR model with multiscale diffusion profiles of WM network links as features to predict the spatial maturation of CT. Spatial maturation of CT and diffusion profiles of WM network links were obtained from CBD dataset.

bioRxiv preprint doi: https://doi.org/10.1101/2022.12.15.520527; this version posted December 15, 2022. The copyright holder for this preprint (which was not certified by peer review) is the author/funder, who has granted bioRxiv a license to display the preprint in perpetuity. It is made available under aCC-BY-NC-ND 4.0 International license.

Table S4 Accuracy to predict the spatial maturation of CT by using multiscale diffusion profiles of network links from HCP-D dataset as features (1000-node resolution).

Neighboring scale	Accuracy	$p_{rewired}$	p_{spin}
1	0.78	<0.001	<0.001
2	0.77	<0.001	<0.001
3	0.77	<0.001	<0.001
4	0.75	<0.001	<0.001
5	0.73	<0.001	<0.001
6	0.71	<0.001	<0.001
7	0.70	<0.001	<0.001
8	0.69	<0.001	<0.001

Note: The table above gives the prediction accuracies and *p*-values (calculated as the fraction of null values exceeding the observed accuracy in the "rewired" test and "spin" test) by using an SVR model with multiscale diffusion profiles of WM network links as features to predict the spatial maturation of CT. The spatial maturation of CT was obtained from CBD dataset. Diffusion profiles of WM network links were obtained from HCP-D dataset.

bioRxiv preprint doi: https://doi.org/10.1101/2022.12.15.520527; this version posted December 15, 2022. The copyright holder for this preprint (which was not certified by peer review) is the author/funder, who has granted bioRxiv a license to display the preprint in perpetuity. It is made available under aCC-BY-NC-ND 4.0 International license.

Table S5 Accuracy to predict the spatial maturation of CT by using multiscale diffusion profiles of network links as features (1000-node resolution, independent tests in HCP-D dataset).

Neighboring scale	Accuracy	$p_{rewired}$	p_{spin}
1	0.66	<0.001	<0.001
2	0.65	<0.001	<0.001
3	0.65	<0.001	<0.001
4	0.60	<0.001	0.015
5	0.57	<0.001	0.152
6	0.55	<0.001	0.206
7	0.53	<0.001	0.313
8	0.51	<0.001	0.439

Note: The table above gives the prediction accuracies and *p*-values (calculated as the fraction of null values exceeding the observed accuracy in the "rewired" test and "spin" test) by using an SVR model with multiscale diffusion profiles of WM network links as features to predict the spatial maturation of CT. Spatial maturation of CT and diffusion profiles of WM network links were both obtained from HCP-D dataset.

bioRxiv preprint doi: https://doi.org/10.1101/2022.12.15.520527; this version posted December 15, 2022. The copyright holder for this preprint (which was not certified by peer review) is the author/funder, who has granted bioRxiv a license to display the preprint in perpetuity. It is made available under aCC-BY-NC-ND 4.0 International license.

Table S6 List of genes showing the highest positive and negative correlations with the dominant likelihood map in the main analysis.

	Genes	Correlation	p_{spin}
Positive	NPHP1	0.66	< 0.001
	FAM133A	0.64	< 0.001
	PPFIA2	0.63	< 0.001
	FAM185A	0.63	< 0.001
	BCL2	0.63	< 0.001
	EID2B	0.62	< 0.001
	CHSY3	0.62	< 0.001
	GRM5	0.62	< 0.001
	CCDC120	0.62	< 0.001
	MLIP	0.62	< 0.001
Negative	SNX24	-0.65	< 0.001
	GNA14	-0.64	< 0.001
	NEFL	-0.64	< 0.001
	SLC7A1	-0.62	< 0.001
	DLC1	-0.61	< 0.001
	GBE1	-0.61	< 0.001
	FAM189B	-0.60	< 0.001
	KANK4	-0.60	< 0.001
	TRADD	-0.60	< 0.001
	DPY19L1	-0.60	0.003

Note: The table above gives the top 10 genes most positively and negatively associated with the dominant likelihood map, respectively. The detailed analysis results for all genes are available at https://github.com/Xinyuan-Liang/SC-shapes-the-maturation-of-cortical-morphology/tree/main/data/gene/AHBA_results.xlsx.

bioRxiv preprint doi: https://doi.org/10.1101/2022.12.15.520527; this version posted December 15, 2022. The copyright holder for this preprint (which was not certified by peer review) is the author/funder, who has granted bioRxiv a license to display the preprint in perpetuity. It is made available under aCC-BY-NC-ND 4.0 International license.

Table S7 Enrichment analysis (GO terms of biological processes and cellular component) reveals significant positive correlations with the dominant likelihood map in the main analysis.

	GO term ID	GO term	Raw *p*-value	*q*_value FDR
Biological Processes	GO:0007611	learning or memory	4.38E-06	1.16E-02
	GO:0050808	synapse organization	6.77E-06	1.16E-02
	GO:0048666	neuron development	9.14E-06	1.16E-02
	GO:0050890	cognition	9.62E-06	1.16E-02
Cellular Component	GO:0098978	glutamatergic synapse	1.22E-08	7.34E-06
	GO:0097060	synaptic membrane	3.55E-08	1.07E-05
	GO:0098794	postsynapse	1.29E-07	2.57E-05
	GO:0045211	postsynaptic membrane	1.71E-07	2.57E-05
	GO:0099240	intrinsic component of synaptic membrane	3.40E-07	4.10E-05
	GO:0043197	dendritic spine	4.80E-07	4.83E-05
	GO:0044309	neuron spine	6.20E-07	5.34E-05
	GO:0098936	intrinsic component of postsynaptic membrane	1.67E-06	1.24E-04
	GO:0099699	integral component of synaptic membrane	1.86E-06	1.24E-04
	GO:0030425	dendrite	2.23E-06	1.29E-04
	GO:0097447	dendritic tree	2.36E-06	1.29E-04
	GO:0032279	asymmetric synapse	5.76E-06	2.90E-04
	GO:0043005	neuron projection	6.72E-06	3.12E-04
	GO:0045202	synapse	7.90E-06	3.40E-04
	GO:0036477	somatodendritic compartment	9.77E-06	3.93E-04

Note: The table above gives the significant enrichment terms for genes that show significant positive correlations with the dominant likelihood map. We used the online tool REViGO (http://revigo.irb.hr) to select the most meaningful GO terms and highlight them. The detailed enrichment analysis results for all genes are available at https://github.com/Xinyuan-Liang/SC-shapes-the-maturation-of-cortical-morphology/tree/main/data/gene/AHBA_results.xlsx.

bioRxiv preprint doi: https://doi.org/10.1101/2022.12.15.520527; this version posted December 15, 2022. The copyright holder for this preprint (which was not certified by peer review) is the author/funder, who has granted bioRxiv a license to display the preprint in perpetuity. It is made available under aCC-BY-NC-ND 4.0 International license.

Table S8 Enrichment analysis (GO terms of biological processes and cellular component) reveals significant negative correlations with the dominant likelihood map in the main analysis.

	GO term ID	GO term	Raw *p*-value	*q*_value FDR
Biological Processes	GO:0019752	carboxylic acid metabolic process	5.39E-10	3.19E-06
	GO:0043436	oxoacid metabolic process	1.56E-09	4.44E-06
	GO:0006082	organic acid metabolic process	2.25E-09	4.44E-06
	GO:0006091	generation of precursor metabolites and energy	3.49E-09	5.16E-06
	GO:0019637	organophosphate metabolic process	5.12E-09	6.05E-06
	GO:0006163	purine nucleotide metabolic process	2.00E-08	1.97E-05
	GO:0009117	nucleotide metabolic process	2.61E-08	2.21E-05
	GO:0006753	nucleoside phosphate metabolic process	3.55E-08	2.62E-05
	GO:0072521	purine-containing compound metabolic process	4.57E-08	3.00E-05
	GO:0045333	cellular respiration	6.86E-08	4.06E-05
	GO:0015980	energy derivation by oxidation of organic compounds	1.24E-07	6.69E-05
	GO:0072522	purine-containing compound biosynthetic process	2.78E-07	1.37E-04
	GO:0009144	purine nucleoside triphosphate metabolic process	5.38E-07	2.36E-04
	GO:0006164	purine nucleotide biosynthetic process	5.57E-07	2.36E-04
	GO:0055086	nucleobase-containing small molecule metabolic process	8.55E-07	3.05E-04
	GO:0009060	aerobic respiration	9.08E-07	3.05E-04
	GO:0009150	purine ribonucleotide metabolic process	9.12E-07	3.05E-04
	GO:1902600	proton transmembrane transport	9.27E-07	3.05E-04
	GO:0006811	ion transport	1.25E-06	3.66E-04
	GO:0009205	purine ribonucleoside triphosphate metabolic process	1.29E-06	3.66E-04
	GO:0019693	ribose phosphate metabolic process	1.30E-06	3.66E-04
	GO:0009152	purine ribonucleotide biosynthetic process	1.60E-06	4.30E-04
	GO:0009141	nucleoside triphosphate metabolic process	1.94E-06	4.72E-04
	GO:0009199	ribonucleoside triphosphate metabolic process	1.99E-06	4.72E-04
	GO:0046390	ribose phosphate biosynthetic process	1.99E-06	4.72E-04
	GO:0009259	ribonucleotide metabolic process	2.37E-06	5.38E-04
	GO:0046034	ATP metabolic process	2.70E-06	5.78E-04
	GO:0006812	cation transport	2.74E-06	5.78E-04
	GO:1901135	carbohydrate derivative metabolic process	3.07E-06	6.25E-04
	GO:0046434	organophosphate catabolic process	3.88E-06	7.65E-04
	GO:0009260	ribonucleotide biosynthetic process	4.46E-06	8.52E-04
	GO:0090407	organophosphate biosynthetic	6.74E-06	1.21E-03

bioRxiv preprint doi: https://doi.org/10.1101/2022.12.15.520527; this version posted December 15, 2022. The copyright holder for this preprint (which was not certified by peer review) is the author/funder, who has granted bioRxiv a license to display the preprint in perpetuity. It is made available under aCC-BY-NC-ND 4.0 International license.

		process		
	GO:0034220	ion transmembrane transport	6.76E-06	1.21E-03
	GO:0022900	electron transport chain	7.56E-06	1.32E-03
	GO:0009165	nucleotide biosynthetic process	8.44E-06	1.43E-03
	GO:1901293	nucleoside phosphate biosynthetic process	8.88E-06	1.46E-03
	GO:0015986	proton motive force-driven ATP synthesis	9.25E-06	1.48E-03
Cellular Component	GO:0043209	myelin sheath	4.29E-16	3.20E-13
	GO:0005743	mitochondrial inner membrane	3.35E-11	1.05E-08
	GO:0019866	organelle inner membrane	4.24E-11	1.05E-08
	GO:0031966	mitochondrial membrane	5.64E-10	1.05E-07
	GO:0005740	mitochondrial envelope	2.07E-09	3.08E-07
	GO:0098798	mitochondrial protein-containing complex	3.16E-09	3.92E-07
	GO:1990204	oxidoreductase complex	3.15E-08	3.35E-06
	GO:0005759	mitochondrial matrix	1.24E-07	1.16E-05
	GO:0031967	organelle envelope	1.60E-07	1.19E-05
	GO:0031975	envelope	1.60E-07	1.19E-05
	GO:0098800	inner mitochondrial membrane protein complex	3.12E-06	2.12E-04

Note: The table above gives the significant enrichment terms for genes that show significant negative correlations with the dominant likelihood map. We used the online tool REViGO (http://revigo.irb.hr) to select the most meaningful GO terms and highlight them. The detailed enrichment analysis results for all genes are available at https://github.com/Xinyuan-Liang/SC-shapes-the-maturation-of-cortical-morphology/tree/main/data/gene/AHBA_results.xlsx.

bioRxiv preprint doi: https://doi.org/10.1101/2022.12.15.520527; this version posted December 15, 2022. The copyright holder for this preprint (which was not certified by peer review) is the author/funder, who has granted bioRxiv a license to display the preprint in perpetuity. It is made available under aCC-BY-NC-ND 4.0 International license.

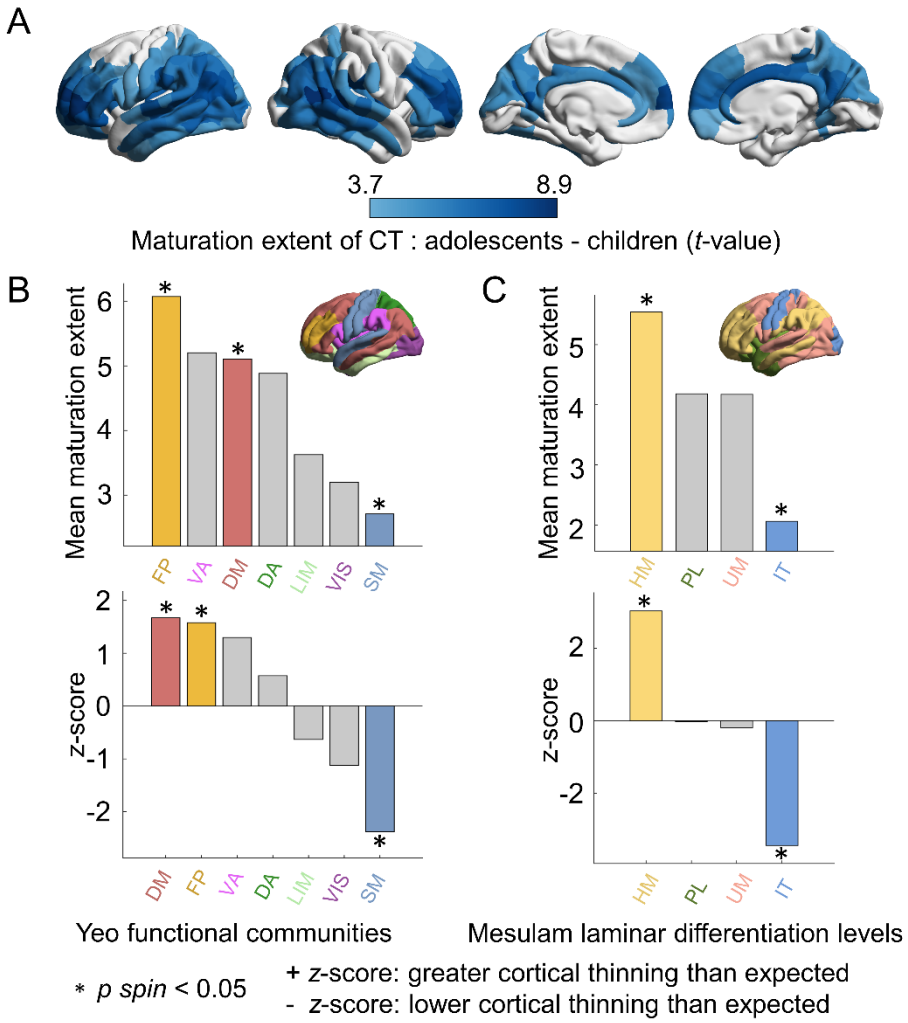

Figure S1. CT maturation from childhood to adolescence at 219-node resolution. (**A**) Spatial maturation map of CT from childhood to adolescence. A greater positive *t* value denotes more pronounced cortical thinning with development. The maps were corrected using a Bonferroni correction method for multiple comparisons ($p_{bonf} < 0.05$). (**B**) The mean CT maturation extent (estimated by *t* value) within each brain community was defined by Yeo et al. (30), and the laminar differentiation level was defined by Mesulam et al. (31) (**C**). Spin tests (32, 33) were performed by spherical projection and rotation class positions 1000 times for correcting spatial autocorrelations, and the class-specific mean *t* values were expressed as *z* scores relative to this null model. A positive *z* score indicated higher cortical thinning than expected by chance. Asterisks denote statistical significance ($p_{spin} < 0.05$). VIS, visual; SM, somatomotor; LIM, limbic; DA, dorsal attention; VA, ventral attention; FP, frontoparietal; DM, default mode; IT, idiotypic; PL, paralimbic; UM, unimodal and HM, heteromodal.

bioRxiv preprint doi: https://doi.org/10.1101/2022.12.15.520527; this version posted December 15, 2022. The copyright holder for this preprint (which was not certified by peer review) is the author/funder, who has granted bioRxiv a license to display the preprint in perpetuity. It is made available under aCC-BY-NC-ND 4.0 International license.

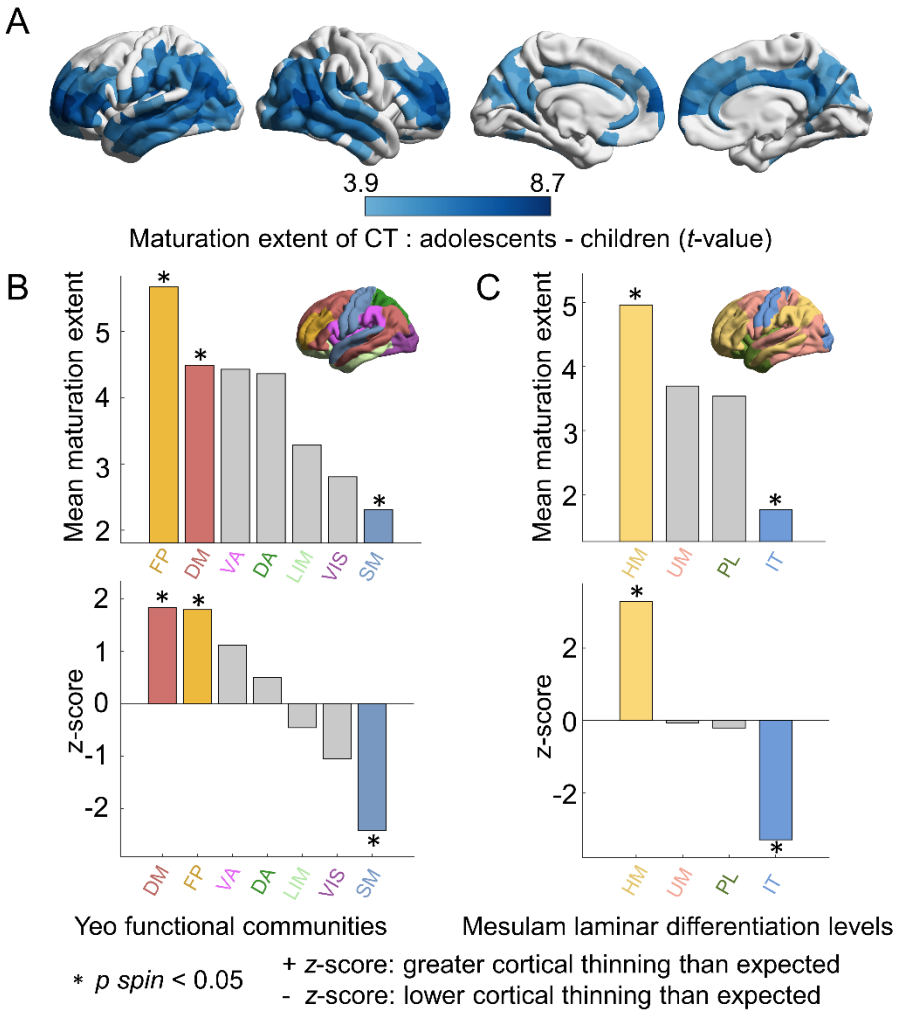

Figure S2. CT maturation from childhood to adolescence at 448-node resolution. (**A**) Spatial maturation map of CT from childhood to adolescence. A greater positive *t* value denotes more pronounced cortical thinning with development. The maps were corrected using a Bonferroni correction method for multiple comparisons ($p_{bonf} < 0.05$). (**B**) The mean CT maturation extent (estimated by *t* value) within each brain community was defined by Yeo et al. (30), and the laminar differentiation level was defined by Mesulam et al. (31) (**C**). Spin tests (32, 33) were performed by spherical projection and rotation class positions 1000 times for correcting spatial autocorrelations, and the class-specific mean *t* values were expressed as *z* scores relative to this null model. A positive *z* score indicated higher cortical thinning than expected by chance. Asterisks denote statistical significance ($p_{spin} < 0.05$). VIS, visual; SM, somatomotor; LIM, limbic; DA, dorsal attention; VA, ventral attention; FP, frontoparietal; DM, default mode; IT, idiotypic; PL, paralimbic; UM, unimodal and HM, heteromodal.

bioRxiv preprint doi: https://doi.org/10.1101/2022.12.15.520527; this version posted December 15, 2022. The copyright holder for this preprint (which was not certified by peer review) is the author/funder, who has granted bioRxiv a license to display the preprint in perpetuity. It is made available under aCC-BY-NC-ND 4.0 International license.

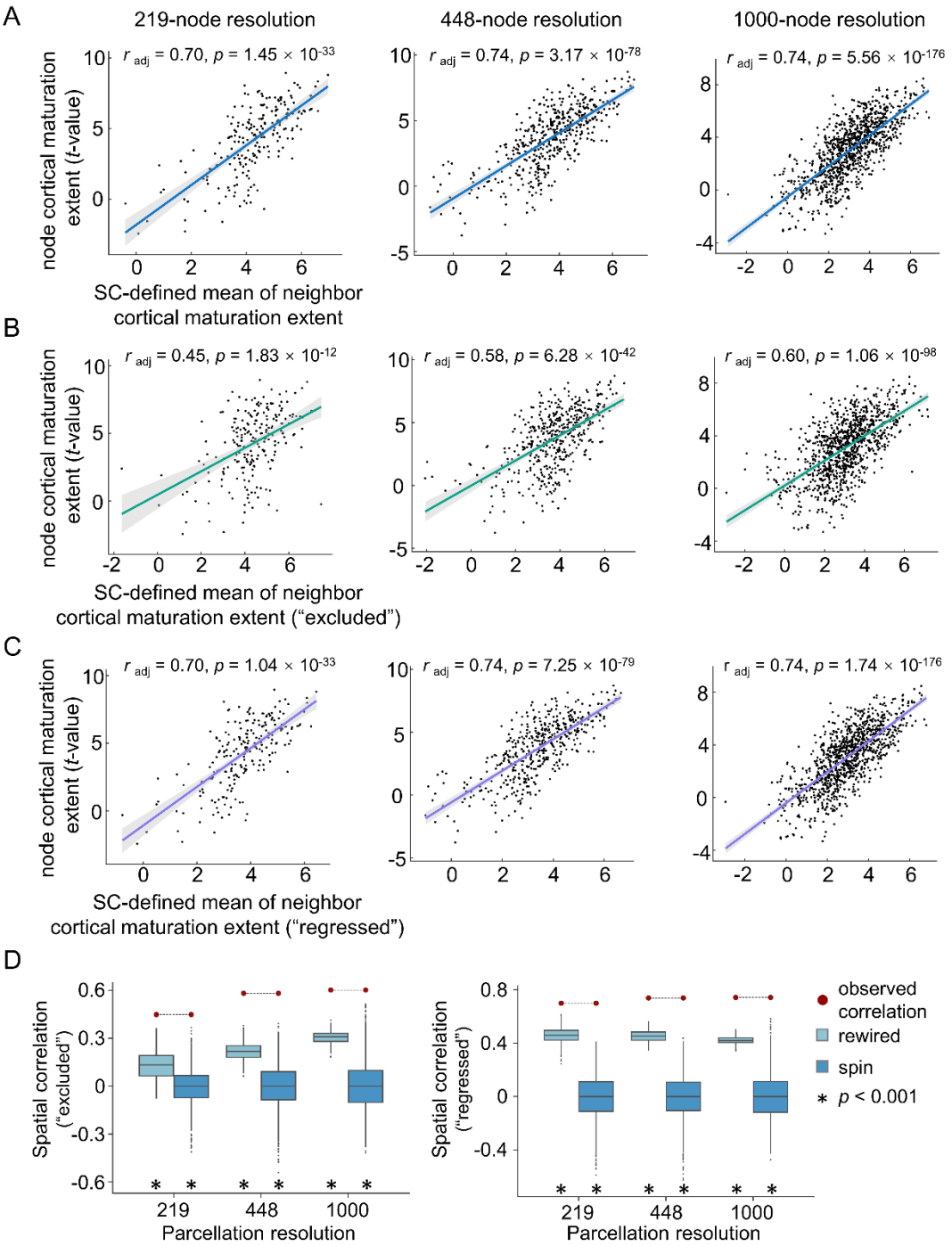

Figure S3. WM network-based CT maturation. (**A**) Significant correlations were observed between the nodal CT maturation extent and the mean of its directly connected neighbors at all three nodal resolutions. To obtain comparable correlation values under different number of observation samples, we calculated the adjusted *r*. (**B**) To determine whether these correlations were driven by the spatial proximity effect, we excluded all spatially adjoining neighbors and recalculated the mean CT maturation extent of the remaining structurally connected neighbors for each brain region ("excluded"), significant correlations were observed after re-estimating at

bioRxiv preprint doi: https://doi.org/10.1101/2022.12.15.520527; this version posted December 15, 2022. The copyright holder for this preprint (which was not certified by peer review) is the author/funder, who has granted bioRxiv a license to display the preprint in perpetuity. It is made available under aCC-BY-NC-ND 4.0 International license.

all three nodal resolutions. (**C**) We regressed out the effect of nodal mean Euclidean distance to its connected neighbors from the mean CT maturation extent ("regressed"), significant correlations were observed after re-estimating at all three nodal resolutions. (**D**) The observed correlations across 3 resolutions (shown as red circles) for "excluded" (left panel) and "regressed" (right panel) analyses were compared against two baseline null models. (1) To determine whether these correlations were driven by the basic spatial embedding of the WM network, we randomly rewired edges while preserving the nodal degree and edge length distribution of the empirical WM network ("rewired", 1000 times, shown as light blue boxes). (2) To determine whether these correlations were driven by spatial autocorrelation, we generated 1000 surrogate maps by rotating region-level cortical *t* values ("spin test", shown as deep blue boxes). Asterisks denote statistical significance ($p < 0.001$).

bioRxiv preprint doi: https://doi.org/10.1101/2022.12.15.520527; this version posted December 15, 2022. The copyright holder for this preprint (which was not certified by peer review) is the author/funder, who has granted bioRxiv a license to display the preprint in perpetuity. It is made available under aCC-BY-NC-ND 4.0 International license.

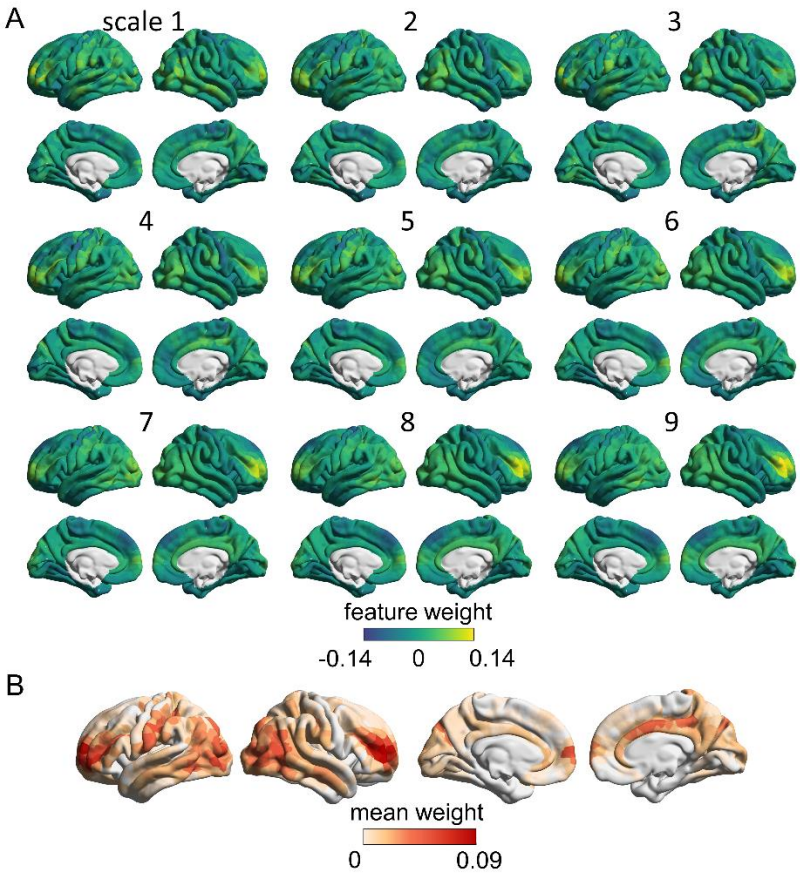

Figure S4. Feature weights for SVR models. (**A**) The feature weights distributions for the SVR model at 1-9 neighboring scales. (**B**) The mean weights of the nine neighboring scales, where nodes with high positive feature weights are mainly located in the frontal and parietal regions.

bioRxiv preprint doi: https://doi.org/10.1101/2022.12.15.520527; this version posted December 15, 2022. The copyright holder for this preprint (which was not certified by peer review) is the author/funder, who has granted bioRxiv a license to display the preprint in perpetuity. It is made available under aCC-BY-NC-ND 4.0 International license.

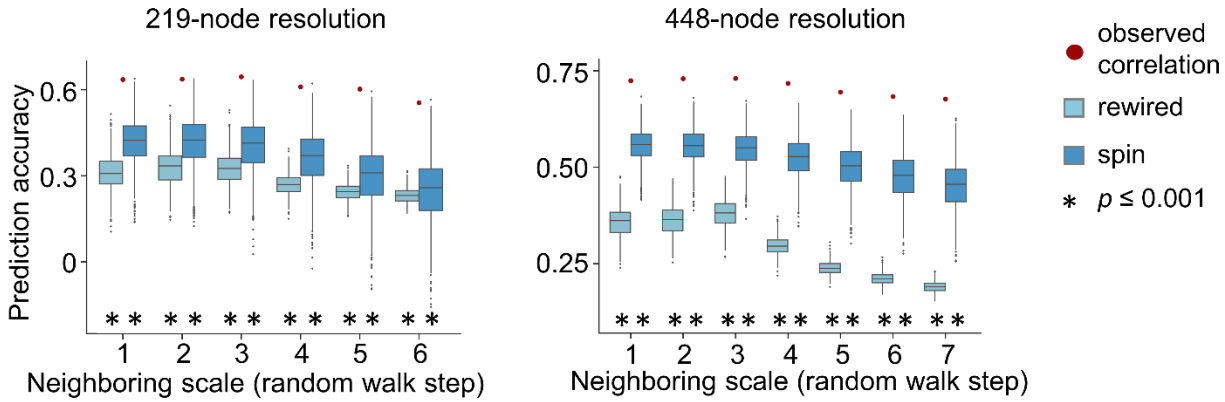

Figure S5. Network-based diffusion model. Significant correlations between the predicted CT maturation and the observed CT maturation at 219-node resolution (left panel) and 448-node resolution (right panel) by using nodal diffusive profiles at multiple neighboring scales as features in SVR model. The observed correlations (red dots) were compared to the correlations obtained from 1000 rewired tests (light blue boxes) and 1000 spin tests (deep blue boxes). Asterisks denote statistical significance (p <= 0.001).

bioRxiv preprint doi: https://doi.org/10.1101/2022.12.15.520527; this version posted December 15, 2022. The copyright holder for this preprint (which was not certified by peer review) is the author/funder, who has granted bioRxiv a license to display the preprint in perpetuity. It is made available under aCC-BY-NC-ND 4.0 International license.

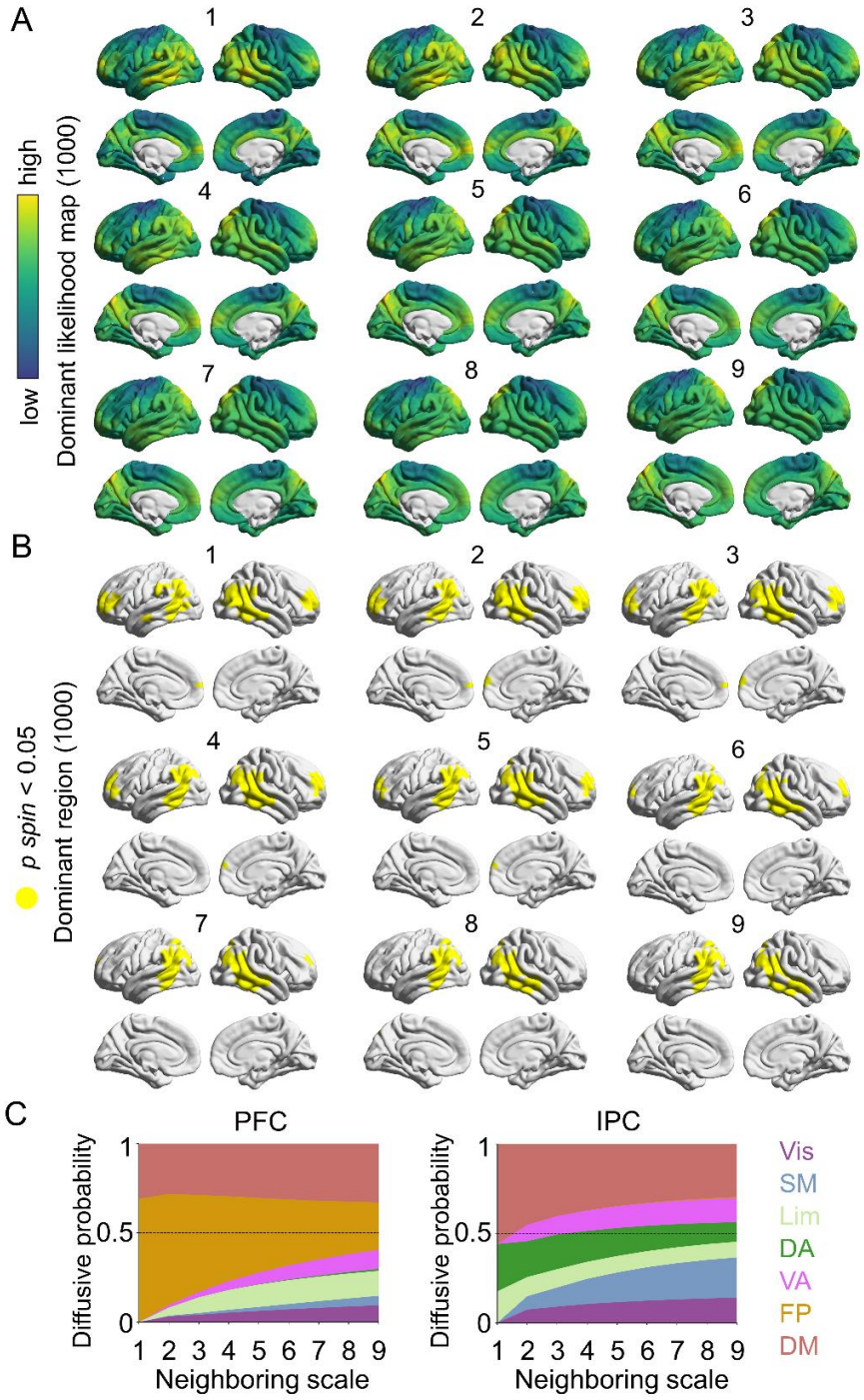

Figure S6. Dominant region results at 1000-node resolution. (**A**) Dominant likelihood distribution maps across multiple neighboring scales at 1000-node resolution. (**B**) Dominant region maps ($p_{spin} < 0.05$) across multiple neighboring scales at 1000-node resolution. (C) Probability of the dominant node located in the prefrontal (left panel) and inferior parietal (right panel) cortex diffusing to each system in the 7 brain communities (30). VIS, visual; SM, somatomotor; LIM, limbic; DA, dorsal attention; VA, ventral attention; FP, frontoparietal; DM, default mode; PFC, prefrontal cortex; IPC, inferior parietal cortex

bioRxiv preprint doi: https://doi.org/10.1101/2022.12.15.520527; this version posted December 15, 2022. The copyright holder for this preprint (which was not certified by peer review) is the author/funder, who has granted bioRxiv a license to display the preprint in perpetuity. It is made available under aCC-BY-NC-ND 4.0 International license.

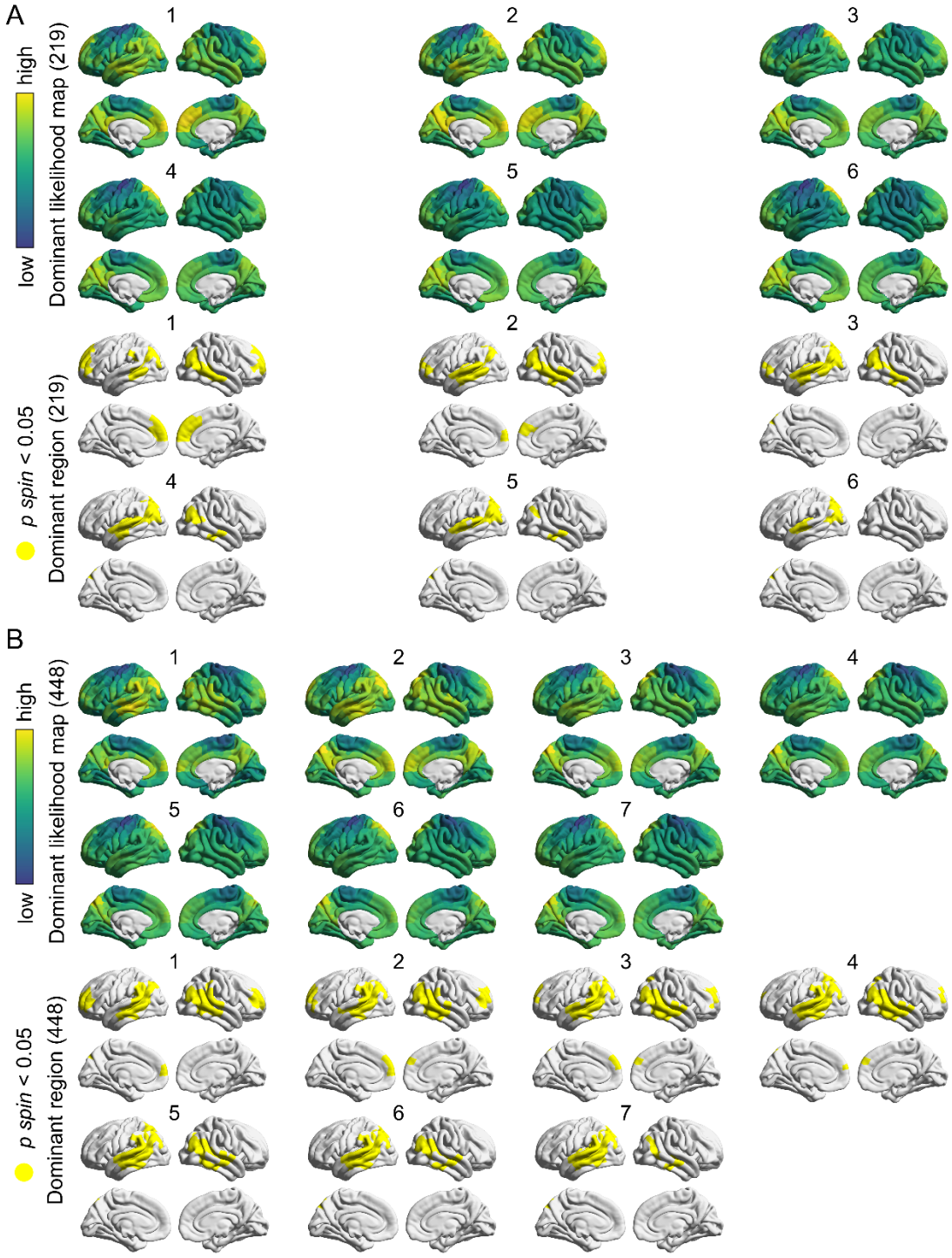

Figure S7. Dominant region results at 219- and 448-node resolution. (**A**) Dominant likelihood distribution maps and dominant region maps ($p_{spin} < 0.05$) across multiple neighboring scales at 219-node resolution. (**B**) Dominant likelihood distribution maps and dominant region maps ($p_{spin} < 0.05$) across multiple neighboring scales at 448-node resolution.

bioRxiv preprint doi: https://doi.org/10.1101/2022.12.15.520527; this version posted December 15, 2022. The copyright holder for this preprint (which was not certified by peer review) is the author/funder, who has granted bioRxiv a license to display the preprint in perpetuity. It is made available under aCC-BY-NC-ND 4.0 International license.

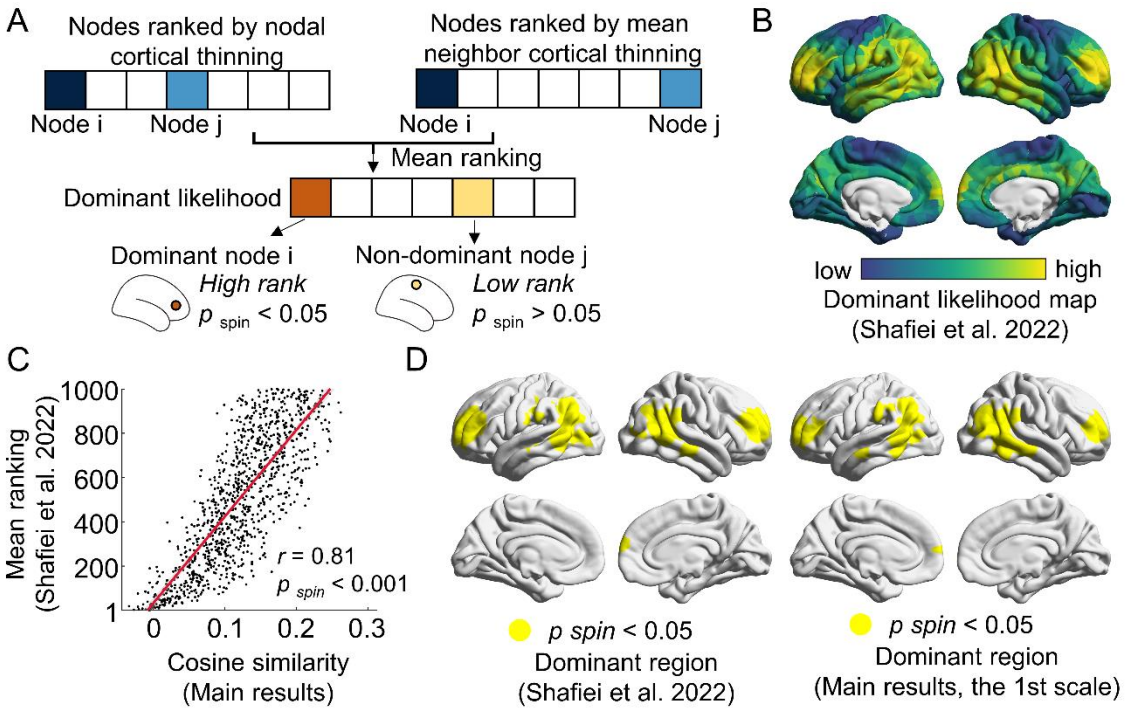

Figure S8. Dominant node identification. (**A**) Dominant likelihood distribution map was obtained by a different identification approach introduced by Shafiei et al. (29), which calculated the mean maturation extents in both themselves and their directly connected neighbors. Regions with significantly higher mean ranks ($p_{spin} < 0.05$) were identified as the dominant nodes. (**B**) Dominant likelihood distribution map at 1000-node resolution. (**C**) The dominant likelihood maps obtained using the approach introduced by Shafiei et al. spatially correlated with the map in our main results (Spearman's $r = 0.81$, $p_{spin} < 0.001$). (**D**) Dominant region map ($p_{spin} < 0.05$, left panel) shows a high similarity to the map (at the 1st neighboring scale) in our main analysis (right panel).

bioRxiv preprint doi: https://doi.org/10.1101/2022.12.15.520527; this version posted December 15, 2022. The copyright holder for this preprint (which was not certified by peer review) is the author/funder, who has granted bioRxiv a license to display the preprint in perpetuity. It is made available under aCC-BY-NC-ND 4.0 International license.

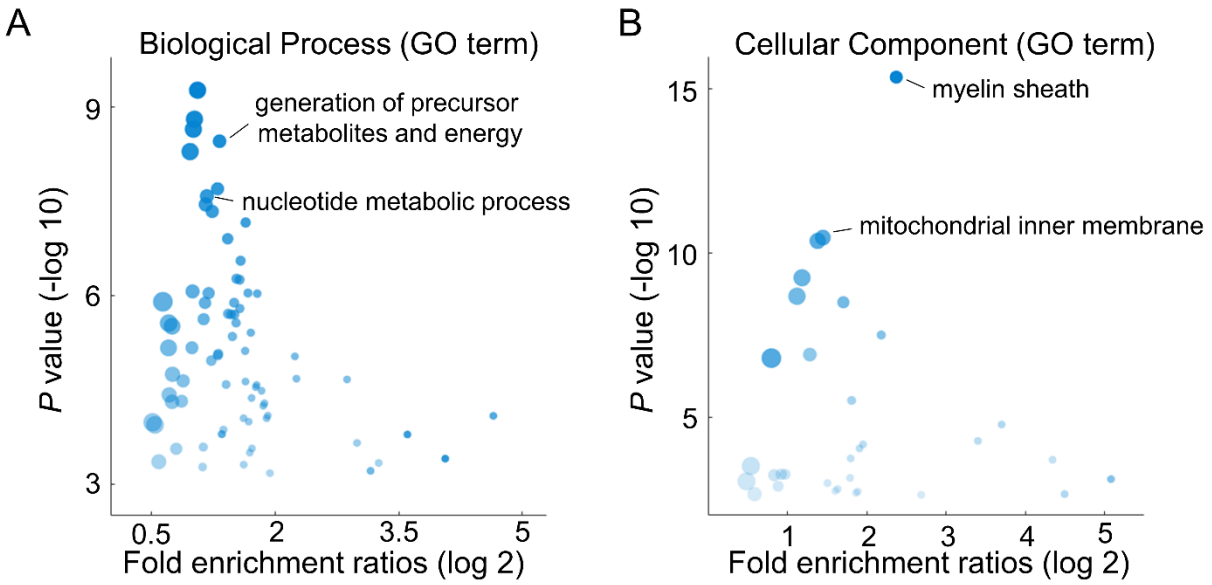

Figure S9. Gene Ontology enrichment results for negatively correlated gene sets. The dots represent the GO terms corrected for multiple comparisons (FDR-corrected, $P < 0.05$). The size of the dot indicates the number of genes belonging to the corresponding GO term, and the transparency of the dot represents the significance of the corresponding GO term.

bioRxiv preprint doi: https://doi.org/10.1101/2022.12.15.520527; this version posted December 15, 2022. The copyright holder for this preprint (which was not certified by peer review) is the author/funder, who has granted bioRxiv a license to display the preprint in perpetuity. It is made available under aCC-BY-NC-ND 4.0 International license.

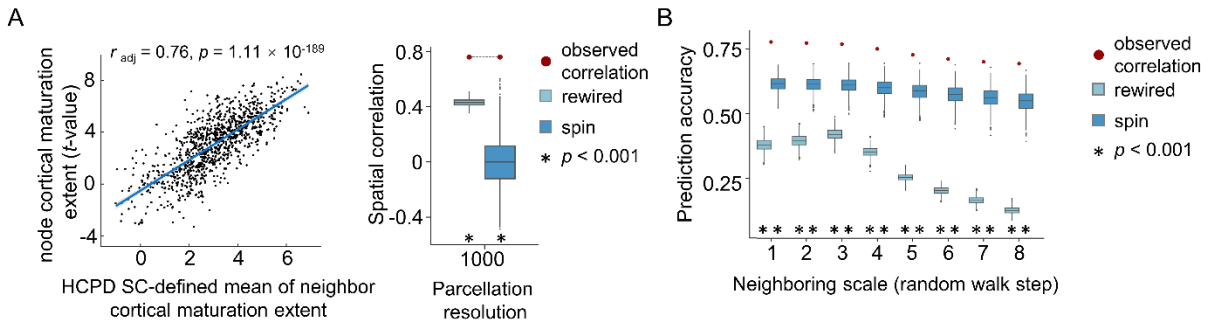

Figure S10. Validation of the WM connectome backbone effectiveness. Diffusion images with multishell diffusion gradients from Replication Dataset (HCP-D) were used to validate the effectiveness of the WM connectome backbone. (**A**) A significant correlation was observed between the nodal CT maturation extent and the mean of its directly connected neighbors at 1000-node resolution (left panel, $r_{adj} = 0.76$, $P = 1.11 \times 10^{-189}$). This observed correlation (red dots) was compared against two baseline null models (right panel). (1) To determine whether these correlations were driven by the basic spatial embedding of the WM network, we randomly rewired edges while preserving the nodal degree and edge length distribution of the empirical WM network ("rewired", 1000 times, shown as light blue boxes). (2) To determine whether these correlations were driven by spatial autocorrelation, we generated 1000 surrogate maps by rotating region-level cortical *t* values ("spin test", shown as deep blue boxes). (**B**) Significant correlations between the predicted CT maturation and the observed CT maturation by using nodal diffusive profiles at multiple neighboring scales as features in the SVR model. These observed correlations (red dots) were compared to the correlations obtained from 1000 rewired tests (light blue boxes) and 1000 spin tests (deep blue boxes). Asterisks denote statistical significance ($p < 0.001$).

bioRxiv preprint doi: https://doi.org/10.1101/2022.12.15.520527; this version posted December 15, 2022. The copyright holder for this preprint (which was not certified by peer review) is the author/funder, who has granted bioRxiv a license to display the preprint in perpetuity. It is made available under aCC-BY-NC-ND 4.0 International license.

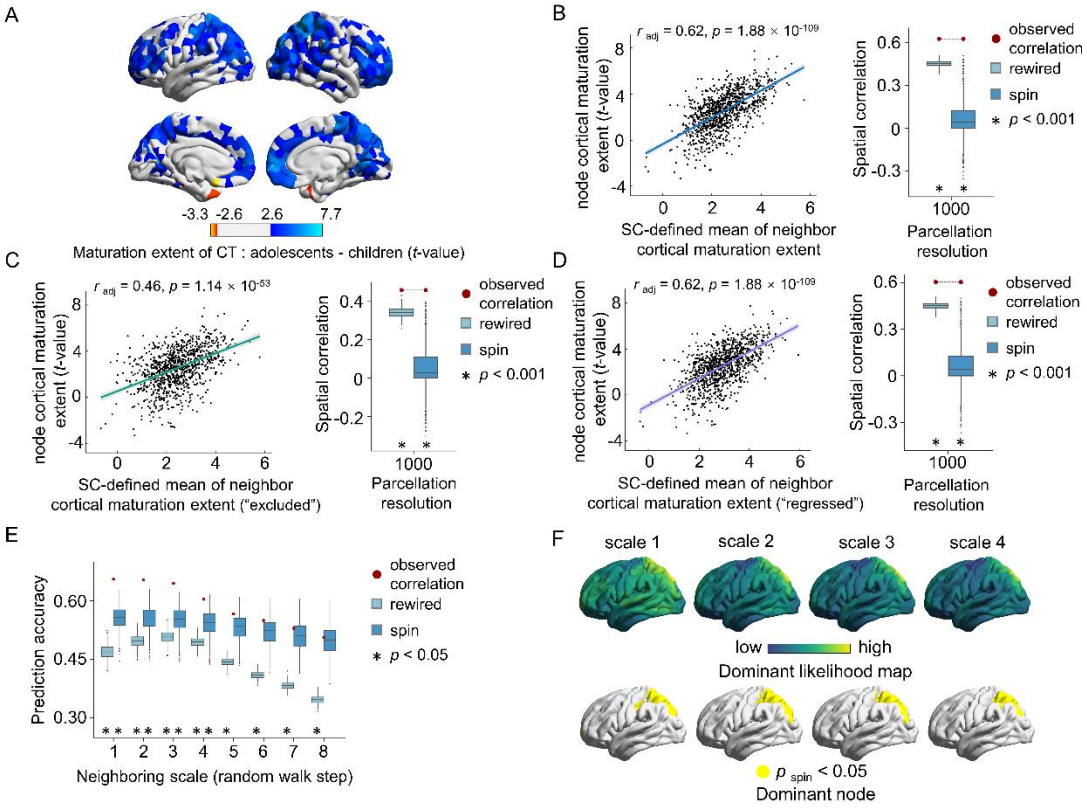

Figure S11. WM network-based CT maturation in Replication Dataset. (**A**) Spatial maturation map of CT from childhood to adolescence at 1000-node resolution ($P < 0.01$). A greater positive *t* value denotes more pronounced cortical thinning with development. (**B**) Significant correlations were observed between the nodal CT maturation extent and the mean of its directly connected neighbors. The observed correlations were compared against two baseline null models. (1) To determine whether these correlations were driven by the basic spatial embedding of the WM network, we randomly rewired edges while preserving the nodal degree and edge length distribution of the empirical WM network ("rewired", 1000 times, shown as light blue boxes). (2) To determine whether these correlations were driven by spatial autocorrelation, we generated 1000 surrogate maps by rotating region-level cortical *t* values ("spin test", shown as deep blue boxes). Asterisks denote statistical significance ($p < 0.001$). Significant correlations were also observed after excluding the spatially adjoining neighbors (**C**) and regressing out the inter-node Euclidean distance (**D**). (**E**) Significant correlations between the predicted CT maturation obtained from the SVR model using nodal diffusive profiles at multiple neighboring scales as features and the observed CT maturation. The observed correlations (red dots) were compared to the correlations obtained from 1000 rewired tests (light blue boxes) and 1000 spin tests (deep blue boxes). Asterisks denote statistical significance ($p < 0.05$). (**F**) Dominant likelihood distribution maps and dominant region maps ($p_{spin} < 0.05$) at 1-4 neighboring scales.